

## Durham Research Online

---

### Deposited in DRO:

14 January 2020

### Version of attached file:

Published Version

### Peer-review status of attached file:

Peer-reviewed

### Citation for published item:

Gillman, S. and Tiley, A.L. and Swinbank, A.M. and Harrison, C.M. and Smail, I. and Dudzeviciute, U. and Sharples, R.M. and Cortese, L. and Obreschkow, D. and Bower, R.G. and Theuns, T. and Cirasuolo, M. and Fisher, D.B. and Glazebrook, K. and Ibar, E. and Mendel, J. T. and Sweet, S.M. (2020) 'From peculiar morphologies to Hubble-type spirals: the relation between galaxy dynamics and morphology in star-forming galaxies at  $z \sim 1.5$ ', *Monthly notices of the Royal Astronomical Society.*, 492 (1). pp. 1492-1512.

### Further information on publisher's website:

<https://doi.org/10.1093/mnras/stz3576>

### Publisher's copyright statement:

This article has been accepted for publication in the *Monthly notices of the Royal Astronomical Society* ©: 2019 The Author(s). Published by Oxford University Press on behalf of the Royal Astronomical Society. All rights reserved.

## Use policy

---

The full-text may be used and/or reproduced, and given to third parties in any format or medium, without prior permission or charge, for personal research or study, educational, or not-for-profit purposes provided that:

- a full bibliographic reference is made to the original source
- a [link](#) is made to the metadata record in DRO
- the full-text is not changed in any way

The full-text must not be sold in any format or medium without the formal permission of the copyright holders.

Please consult the [full DRO policy](#) for further details.

# From peculiar morphologies to Hubble-type spirals: the relation between galaxy dynamics and morphology in star-forming galaxies at $z \sim 1.5$

S. Gillman<sup>1</sup>,<sup>★</sup> A. L. Tiley<sup>1,2</sup> A. M. Swinbank<sup>1</sup> C. M. Harrison,<sup>3</sup> Ian Smail<sup>1</sup>,  
U. Dudzevičiūtė<sup>1</sup> R. M. Sharples,<sup>1,4</sup> L. Cortese<sup>2,5</sup> D. Obreschkow<sup>2,6</sup>  
R. G. Bower<sup>1,7</sup> T. Theuns,<sup>7</sup> M. Cirasuolo,<sup>3</sup> D. B. Fisher<sup>8</sup> K. Glazebrook,<sup>8</sup>  
Edo Ibar,<sup>9</sup> J. Trevor Mendel<sup>10</sup> and Sarah M. Sweet<sup>5,8</sup>

<sup>1</sup>Centre for Extragalactic Astronomy, Durham University, South Road, Durham DH1 3LE, UK

<sup>2</sup>International Centre for Radio Astronomy Research, University of Western Australia, 35 Stirling Highway, Crawley, WA 6009, Australia

<sup>3</sup>European Southern Observatory, Karl-Schwarzschild-Str 2, D-85748 Garching b. München, Germany

<sup>4</sup>Centre for Advanced Instrumentation, Durham University, South Road, Durham DH1 3LE, UK

<sup>5</sup>ARC Centre of Excellence for All Sky Astrophysics in 3 Dimensions (ASTRO 3D)

<sup>6</sup>Australian Research Council Centre of Excellence for All-Sky Astrophysics, 44 Rosehill Street Redfern, NSW 2016, Australia

<sup>7</sup>Institute for Computational Cosmology, Durham University, South Road, Durham DH1 3LE, UK

<sup>8</sup>Centre for Astrophysics and Supercomputing, Swinburne University of Technology, PO Box 218, Hawthorn, VIC 3122, Australia

<sup>9</sup>Instituto de Física y Astronomía, Universidad de Valparaíso, Avda. Gran Bretaña 1111, Valparaíso, Chile

<sup>10</sup>Research School of Astronomy and Astrophysics, Australian National University, Canberra, ACT 2611, Australia

Accepted 2019 December 18. Received 2019 December 13; in original form 2019 October 8

## ABSTRACT

We present an analysis of the gas dynamics of star-forming galaxies at  $z \sim 1.5$  using data from the KMOS Galaxy Evolution Survey. We quantify the morphology of the galaxies using *HST* CANDELS imaging parametrically and non-parametrically. We combine the  $H\alpha$  dynamics from KMOS with the high-resolution imaging to derive the relation between stellar mass ( $M_*$ ) and stellar specific angular momentum ( $j_*$ ). We show that high-redshift star-forming galaxies at  $z \sim 1.5$  follow a power-law trend in specific stellar angular momentum with stellar mass similar to that of local late-type galaxies of the form  $j_* \propto M_*^{0.53 \pm 0.10}$ . The highest specific angular momentum galaxies are mostly disc-like, although generally both peculiar morphologies and disc-like systems are found across the sequence of specific angular momentum at a fixed stellar mass. We explore the scatter within the  $j_* - M_*$  plane and its correlation with both the integrated dynamical properties of a galaxy (e.g. velocity dispersion, Toomre  $Q_g$ ,  $H\alpha$  star formation rate surface density  $\Sigma_{\text{SFR}}$ ) and its parametrized rest-frame UV/optical morphology (e.g. Sérsic index, bulge to total ratio, clumpiness, asymmetry, and concentration). We establish that the position in the  $j_* - M_*$  plane is strongly correlated with the star-formation surface density and the clumpiness of the stellar light distribution. Galaxies with peculiar rest-frame UV/optical morphologies have comparable specific angular momentum to disc-dominated galaxies of the same stellar mass, but are clumpier and have higher star formation rate surface densities. We propose that the peculiar morphologies in high-redshift systems are driven by higher star formation rate surface densities and higher gas fractions leading to a more clumpy interstellar medium.

**Key words:** galaxies: evolution – galaxies: high-redshift – galaxies: kinematics and dynamics.

## 1 INTRODUCTION

In 1926, Edwin Hubble established the Hubble-Sequence of galaxy morphology by visually classifying local galaxies into distinct classes of spirals, ellipticals, lenticulars, and peculiars (Hubble 1926). The Hubble-Sequence remains one of the defining

\* E-mail: [steven.r.gillman@durham.ac.uk](mailto:steven.r.gillman@durham.ac.uk)

characteristics of galaxies, and provides one of the key constraints that galaxy formation models strive to reproduce (e.g. Tissera & Lambas 1990; Snyder et al. 2015; Trayford et al. 2018, Zoldan et al. 2019). As originally suggested by Sandage, Freeman & Stokes (1970), dynamical surveys of local galaxies suggest that the Hubble-Sequence of galaxy morphologies follows a sequence of increasing angular momentum at a fixed mass (e.g. Sandage 1986; Hernandez & Cervantes-Sodi 2006; Hammer & Images Collaboration 2009; Falcón-Barroso, Lyubenova & van de Ven 2015).

In the cold dark matter paradigm, galaxies form at the centres of dark matter haloes. As the dark matter haloes grow early in their formation history, they acquire angular momentum ( $J$ ) as a result of large-scale tidal torques that arise from the growth of perturbations (Stewart et al. 2017). The specific angular momentum acquired has a strong mass dependence, with  $j \propto M_{\text{halo}}^{2/3}$  (e.g. Catelan & Theuns 1996). As the gas collapses within the halo from the virial radius to the disc scale, the baryons can both lose and gain angular momentum. The models suggest that late-type galaxies (e.g. star-forming, discy, dynamically young systems) are those that better preserve the halo dynamical properties. The (weak) conservation of baryonic angular momentum during collapse results in a centrifugally supported disc with an exponential mass profile (e.g. Mo, Mao & White 1998). Early-type galaxies, in contrast, have either a very low retention factor of the baryonic angular momentum (e.g. D’Onghia et al. 2006; Sokolowska et al. 2017) or reside in dark matter haloes with low spin, likely due to mergers and disc instabilities (e.g. Hernandez et al. 2007; Rodriguez-Gomez et al. 2017).

Fall & Efstathiou (1980) established that the specific stellar angular momentum,  $j_* = J/M_*$ , of low-redshift massive disc galaxies follows a tight sequence with stellar mass quantified as  $j_* \propto M_*^{2/3}$ . This  $j_* - M_*$  plane was shown by Romanowsky & Fall (2012) to correlate with galaxy morphology, with early-type galaxies having a factor of  $\sim 5\times$  less specific angular momentum than late-type galaxies of the same stellar mass. More recent integral field studies of low-redshift galaxies have analysed the connection between a galaxy’s parametrized morphology (e.g. Sérsic index, stellar bulge to total ratio) and specific angular momentum (Obreschkow & Glazebrook 2014; Cortese et al. 2016). More bulge-dominated galaxies, with higher Sérsic indices, have been shown to have lower specific angular momentum at fixed stellar mass (Fall & Romanowsky 2018). The scatter about the  $j_* \propto M_*^{2/3}$  sequence in the local Universe is driven by the variation in the combination of disc and bulge components that make up star-forming late-type galaxies at  $z \sim 0$  (e.g. Romeo & Mogotsi 2018; Sweet et al. 2018; Jadhav Y & Banerjee 2019).

While the role of angular momentum in locating galaxies along the Hubble-Sequence is well constrained at  $z \sim 0$ , the relationship between angular momentum and the emergence of the Hubble-Sequence at high redshift is less established. Early work by Puech et al. (2007) established that star-forming galaxies at intermediate redshifts ( $z \sim 0.6$ ) have comparable dynamical properties to local galaxies. Galaxies identified to have complex kinematics however exhibit significantly more scatter in dynamical scaling relations, with higher levels of turbulence indicating the presence of mergers and interactions. At higher redshift, morphological and dynamical studies have shown that the high-redshift ( $z \sim 2$ ) star-forming galaxy population is dominated by turbulent, gas-rich systems (e.g. Bouché et al. 2007; Genzel et al. 2011; Wisnioski, Förster Schreiber & Wuyts 2015). Multiwavelength imaging has been used to identify a transformation in galaxy morphology from

single-component systems (bulge or disc) to two-component (bulge and disc) systems around  $z \sim 2$  (e.g. Sachdeva et al. 2019). The transition in morphology is reflected in other galaxy properties such as star formation, colour, and stellar mass, indicating there is a wider physical mechanism responsible for the galaxies’ evolution (e.g. Bruce et al. 2014; Lang et al. 2014; Huertas-Company et al. 2015). The transition from a population dominated by clumpy, irregular morphologies to morphologically smooth, disc-like galaxies appears to occur around  $z \sim 1.5$ . This epoch has therefore been heralded as the epoch when the Hubble-Sequence ‘emerged’ (e.g. Cowie, Hu & Songaila 1995; Conselice et al. 2011).

Numerical simulations, which attempt to model the galaxies across cosmic time, suggest that the transition from galaxies with clumpy, irregular visual morphologies to well-defined Hubble-like morphologies is also dependent on the strength and efficiency of feedback controlling star formation (e.g. Benson et al. 2003; Okamoto et al. 2005; Sales et al. 2010). The stellar mass and specific angular momentum of the galactic disc grows as a consequence of the ongoing feedback and cosmological accretion, such that the disc is stable against large-scale collapse (Bournaud et al. 2014; Oklopčić et al. 2017). In particular, the Evolution and Assembly of GaLaxies and their Environments (EAGLE; Crain et al. 2015, Schaye et al. 2015) hydrodynamic simulation has suggested that the morphology of galaxies of all masses at high-redshift are asymmetric, with a causal relationship between the morphology of a galaxy and its host dark matter halo (e.g. Trayford et al. 2018; Thob et al. 2019). The scatter in the angular momentum of the baryons and stars within the EAGLE simulation correlates strongly with other galaxy properties such as gas fraction, stellar concentration, and the ratio of circular velocity to velocity dispersion (Lagos et al. 2017). Recent semi-analytical models have further identified the relation between stellar and halo specific angular momentum exhibiting no redshift evolution (e.g. Marshall et al. 2019), while the relationship between specific angular momentum and stellar mass increases by 0.5 dex from  $z = 7$  to  $z = 2$ , with the dominant morphological fraction of high-redshift galaxies being bulge-dominated systems (e.g. Zoldan et al. 2018, 2019; Tacchella et al. 2019).

Other high-resolution hydrodynamical zoom-in simulations, such as Feedback in Realistic Environments (FIRE; Hopkins et al. 2014, 2018), have shown that the stellar morphology and kinematics of Milky Way mass galaxies at low redshift correlate strongly with the gaseous history of the galaxy and less with the dark matter halo properties. In these simulations the likelihood of the formation of a well-ordered stellar discs below  $z \sim 1$  depends on the gas mass within the disc (e.g. Garrison-Kimmel et al. 2018) as well as the angular momentum of the system (e.g. Obreschkow et al. 2016; El-Badry et al. 2018).

Most of the measurements of the internal dynamics of galaxies at this epoch, which are needed to test these models, have come from moderately small samples of a few tens of galaxies (e.g. Förster Schreiber et al. 2006, Contini et al. 2016, Posti et al. 2018), making it difficult to constrain the physical processes driving the evolution in galaxy dynamics. Larger samples of high-redshift star-forming galaxy dynamics are becoming more available due to the next generation of extragalactic integral field surveys. For example, the KMOS<sup>3D</sup> survey (Wisnioski et al. 2015) of  $\sim 360$  star-forming galaxies at  $z \sim 1-3$  established that the specific angular momentum of a disc galaxy reflects that of its host dark matter halo with the presence of a  $j_* - M_*$  plane at this epoch (Burkert et al. 2016). By analysing the H  $\alpha$  gas dynamics of  $\sim 700$  star-forming galaxies from the KMOS Redshift One Spectroscopic Survey (KROSS; Stott et al. 2016), Harrison et al. (2017) showed that the normalization of the

$j_* - M_*$  plane at  $z \sim 1$  was 0.2–0.3 dex lower compared to that of  $z \sim 0$  disc galaxies, indicating that high-redshift galaxies, at fixed stellar mass, have lower specific stellar angular momentum. It should be noted however that Marasco et al. (2019) concluded that there is no evolution in  $j_* - M_*$  plane from  $z = 0$  in a small selected sample of  $z = 1$  disc galaxies.

The connection between galaxy morphology and the distribution of angular momentum at  $z \sim 0.5$ – $1.5$  was qualitatively established by Swinbank et al. (2017), showing that galaxies with ‘visually’ more disc-dominated morphologies had higher angular momentum at fixed stellar mass while lower angular momentum galaxies had more peculiar ‘complicated’ morphologies. This relationship was quantified further by Harrison et al. (2017), who parametrized the morphology of the KROSS galaxies with Sérsic profiles, establishing a trend of decreasing specific angular momentum, at fixed stellar mass, with increasing Sérsic index, suggesting there is a causal connection between morphology and angular momentum. Merger events and interactions also enhance gas velocity dispersion and reduce a galaxy’s angular momentum, introducing significant scatter into dynamical scaling relations (e.g. Puech et al. 2019).

In order to quantify how the angular momentum of high-redshift star-forming galaxies affects the emergence of the Hubble-type disc galaxies, and the role feedback plays in defining a galaxy’s morphology, we require two key quantities. First, we need to derive the internal dynamics and second, we need to measure rest-frame optical morphology of the galaxies at this epoch both, parametrically and non-parametrically, which requires high-resolution multiwavelength imaging of the galaxies.

In this paper, we present and analyse the relation between gas dynamics, angular momentum, and rest-frame optical morphology in a sample of 235 mass-selected star-forming galaxies in the redshift range  $z = 1.22$ – $1.76$ . This survey, the KMOS Galaxy Evolution Survey (KGES; Tiley et al., in preparation), represents a 27-night guaranteed time programme using the  $K$ -band Multi Object Spectrograph (KMOS; Sharples et al. 2013) which primarily targets star-forming galaxies in the *HST* Cosmic Assembly Near-infrared Deep Extragalactic Legacy Survey (CANDELS; Koekemoer et al. 2011) with multiwavelength imaging. We present the seeing-limited resolved  $H\alpha$  dynamics of 235 galaxies, across a broad range of stellar mass and  $H\alpha$  star formation rate, from which we measure each galaxy’s dynamics and morphology. We analyse the connection between a galaxy’s rest-frame optical morphology, quantified both parametrically and non-parametrically, and its fundamental dynamical properties that define the emergence of the Hubble-Sequence at  $z \sim 1.5$ .

In Section 2, we discuss the sample selection, observations, and data reduction of the KMOS observations that make up the KGES Survey. In Section 3, we derive the galaxy-integrated photometric and morphological properties, e.g. star formation rates, stellar mass, Sérsic index, and stellar continuum sizes. We then use the stellar continuum sizes and inclinations to derive the dynamical properties of the galaxies before combining the galaxy sizes, stellar masses, and dynamical properties to measure the specific angular momentum of the KGES galaxies. In Section 4, we discuss and interpret our findings, exploring the connection between galaxy morphology and dynamics, before giving our conclusions in Section 5.

A nine-year Wilkinson Microwave Anisotropy Probe (Hinshaw et al. 2013) cosmology is used throughout this work with  $\Omega_\Lambda = 0.721$ ,  $\Omega_m = 0.279$ , and  $H_0 = 70 \text{ km s}^{-1} \text{ Mpc}^{-1}$ . In this cosmology a spatial resolution of 0.65 arcsec (the median FWHM of the seeing in our data) corresponds to a physical scale of 5.6 kpc at a redshift of  $z = 1.5$ . All quoted magnitudes are on the AB system

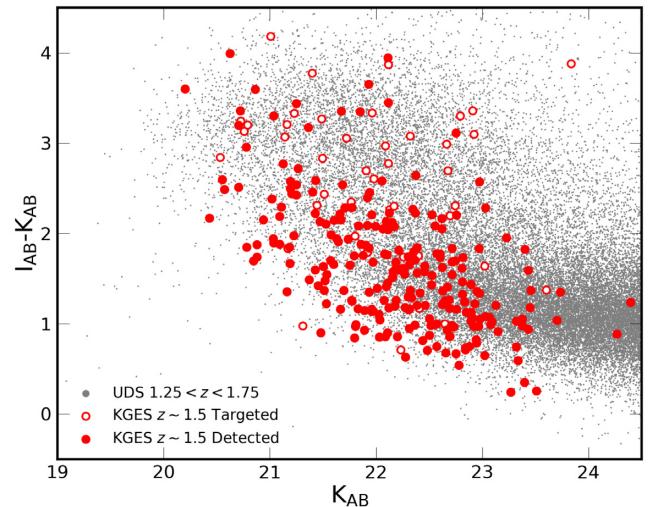


**Figure 1.** The observed  $(I_{AB} - K_{AB})$  colour as a function of the observed  $K$ -band magnitude for the KGES sample. Galaxies detected in  $H\alpha$  are indicated by the red points (243 galaxies). The open symbols represent the 45 galaxies where the  $H\alpha$  signal to noise (S/N) is less than five. Star-forming galaxies in the UDS field in the redshift range  $1.25 < z < 1.75$  are shown for comparison (grey points).

and stellar masses are calculated assuming a Chabrier initial mass function (IMF) (Chabrier 2003).

## 2 SAMPLE SELECTION, OBSERVATIONS, AND DATA REDUCTION

The KMOS Galaxy Evolution Survey (Tiley et al., in preparation) concentrates on measuring the dynamics of main-sequence star-forming galaxies at  $z \sim 1.5$ , and builds upon previous high-redshift surveys of star-forming galaxies (e.g. KROSS at  $z \sim 0.9$ , Stott et al. 2016; Harrison et al. 2017). We predominately target galaxies at  $z \sim 1.5$  in the *HST* CANDELS field within the spectral range containing the redshifted  $H\alpha$   $\lambda 6563$  and  $[N II]$  ( $\lambda 6548$ ,  $\lambda 6583$ ) nebular emission line to obtain a measure of the galaxies’ ongoing star formation. The majority of galaxies in the KGES survey are selected to have known spectroscopic redshifts and a  $K$ -band magnitude of  $K < 22.5$ . If not enough galaxies pass this criteria to fill the KMOS arms in each mask, fainter galaxies were selected. We note that there was no morphological selection when selecting galaxies to be observed with KMOS. In Fig. 1, we show an  $I$ – $K$  colour–magnitude diagram for targeted and  $H\alpha$ -detected KGES galaxies. The galaxies in the survey occupy a similar region of colour–magnitude parameter space to typical star-forming galaxies in the UKIDSS Ultra-Deep Survey (UDS; Lawrence et al. 2007) field from  $z = 1.25$  to  $1.75$ .

A full description of the survey design, observations, and data reduction is presented in Tiley et al. (in preparation). In brief, we observed 288 high-redshift galaxies with KMOS as part of the KGES survey between October 2016 and January 2018. Each target was observed in five observing blocks (OB) for a total exposure time of 27ks in an ABAABA sequence (A = Object frame, B = Sky frame) with individual exposures of 600s. The median FWHM of the seeing in our observations is  $\langle \text{FWHM} \rangle = 0.65 \pm 0.11$  arcsec with a range from FWHM = 0.49 to 0.82 arcsec. Our targets lie in the UDS, Cosmological Evolution Survey (COSMOS; Scoville et al. 2007) and Extended Chandra Deep Field South (ECDFS; Giacconi et al. 2001) extragalactic fields.



The European Southern Observatory (ESO) Recipe Execution Tool (ESOREX; ESO CPL Development Team 2015) pipeline was used to extract, wavelength calibrate, and flat-field each of the spectra and form a data cube from each observation. The sky-subtraction for the KGES observations is performed on a frame-by-frame basis, with an initial A–B subtraction. Before stacking, we employ the Zurich Atmospheric Purge (ZAP; Soto et al. 2016) tool, adapted for use with KMOS, which uses a principal component analysis to characterize and remove the remaining sky residuals in the observations (Mendel et al., in preparation). ZAP is trained on residual sky spectra devoid of source emission derived from a median of the A–B frames.

The final data cube was generated by centring the individual frames according to the position of the point spread function (PSF) star, and then using an iterative  $3\sigma$  clip mean average to reject pixels with cosmic ray contamination. For flux calibration, standard stars were observed each night either immediately before or after the science exposures. These were reduced in an identical manner to the science observations. Of the 288 observed galaxies, 243 were detected in  $H\alpha$  emission and 235 have spatially resolved  $H\alpha$  emission with a median redshift of  $\langle z \rangle = 1.48 \pm 0.01$  ranging from  $z = 1.22$ – $1.76$ .

### 3 ANALYSIS AND RESULTS

In the following sections we discuss galaxy-integrated properties [e.g. stellar mass ( $M_*$ ) and star-formation ( $\dot{M}_*$ ), stellar continuum half-light radius ( $R_h$ ) and Sérsic index ( $n$ )]. We then measure the galaxy dynamics and use the morphological properties, such as stellar continuum half-light radius, to extract and analyse the galaxies’ kinematic information.

#### 3.1 Stellar masses and star formation rates

Our targets were selected to lie in the ECDFS, UDS, and COSMOS extragalactic fields prioritizing the *HST* CANDELS regions and therefore having a wealth of ancillary photometric data available. This allows us to construct spectral energy distributions (SEDs) for each galaxy spanning from the rest-frame *UV* to mid-infrared with photometry from UDS (Almaini et al. 2007), COSMOS (Muzzin et al. 2013), and ECDFS (Giacconi et al. 2001).

To measure the galaxy-integrated properties we derive the multiwavelength photometry from *UV*– $8\mu\text{m}$  by cross-correlating the galaxies in the KGES survey with the catalogues from the surveys listed above. The median of the *U*-, *I*-, and *K*-band magnitude of the sample is  $\langle U_{AB} \rangle = 24.7 \pm 0.06$ ,  $\langle I_{AB} \rangle = 23.7 \pm 0.04$ , and  $\langle K_{AB} \rangle = 22.2 \pm 0.06$ . We then use the MAGPHYS (da Cunha et al. 2008, 2015) code to fit spectral templates to the spectrum of each galaxy from which we derive stellar masses and dust attenuation factors ( $A_v$ ) (Dudzevičiūtė et al., in preparation). The full stellar mass range of our sample is  $\log(M_*[M_\odot]) = 8.9$ – $11.7$  with a median of  $\log(M_*[M_\odot]) = 10.0 \pm 0.1$ . We employ a homogeneous stellar mass uncertainty of  $\pm 0.2$  dex throughout this work that conservatively accounts for the uncertainties in stellar mass values derived from SED fitting of high-redshift star-forming galaxies (Mobasher et al. 2015). We show the SEDs and MAGPHYS fits for all galaxies in Appendix A.

The star formation rates of the galaxies in our sample are derived from the intensity of the summed  $H\alpha$  emission-line fluxes in 2.4 arcsec diameter apertures in the KMOS observations. Following Wuyts et al. (2013), we convert the dust attenuation ( $A_v$ ), derived from MAGPHYS SED fit for each galaxy, to a gas extinction correction

factor. We assume a uniform uncertainty of  $\pm 0.3$  mag on the  $A_v$  of each galaxy to ensure the systematics in deriving dust attenuation factors from SED fitting are accounted for (Muzzin et al. 2009). We then derive extinction-corrected star formation rates for each galaxy following Calzetti et al. (2000). The median  $H\alpha$  star formation rate of the galaxies in our sample is  $\langle \text{SFR} \rangle = 17 \pm 2 M_\odot \text{ yr}^{-1}$  with a 16–84th percentile range of 3–44  $M_\odot \text{ yr}^{-1}$ .

The  $H\alpha$  star formation rates and stellar masses for the KGES sample are shown in Fig. 2. For comparison we also show the KROSS  $z \sim 0.9$  sample (Harrison et al. 2017) as well as 0.1, 1, and  $10\times$  the ‘main-sequence’ for  $z = 1.5$  star-forming galaxies derived in Schreiber et al. (2015). The KGES sample is offset to higher  $H\alpha$  star formation rates compared with KROSS and reflects the increase in the cosmic star formation rate density at this epoch. We conclude that the galaxies in our sample at  $z \sim 1.5$  are representative of the star formation main-sequence at this redshift.

#### 3.2 Galaxy morphology

To investigate the correlation between specific stellar angular momentum and morphology we need to quantify the morphology of the galaxies in our sample as well as derive their stellar continuum half-light radii. There are a variety of different approaches to classify a galaxy’s morphology and in this section we derive both parametric and non-parametric classifications.

We first discuss the derivation and calibration of the Sérsic index and stellar continuum half-light radius, using the GALFIT software (Peng et al. 2011), as well as analysis of the galaxy’s axis ratios and inclinations. To quantify the morphologies non-parametrically, we also measure the concentration, asymmetry, and clumpiness (CAS; Abraham et al. 1996; Conselice 2014) parameters for the galaxies in the KGES survey.

All of the galaxies in the sample were selected from the extragalactic deep fields, either UDS, COSMOS, or ECDFS. Just over half the sample (162 galaxies) are part of the CANDELS survey, and so have deep imaging in *VIJH* wavelength bands, while 94 more have *HST* archival imaging (mostly ACS *I* band). For the remaining 32 galaxies we use ground-based imaging to derive the morphological properties of the galaxies.

The breakdown of broad-band imaging available for the KGES sample, and the PSF half-light radius in each band, is given in Table 1. At  $z = 1.5$ , the observed near-infrared samples the rest frame *V*-band emission, red-ward of the 4000 Å break. To estimate the extent of the stellar light distribution, we use the longest wavelength *HST* or ground-based image available.

##### 3.2.1 Sérsic index and stellar continuum size

We model the stellar light distributions of galaxies in the KGES sample, within  $10 \times 10$  arcsec cut-outs, using the GALFIT software (Peng et al. 2011) which fits single Sérsic profiles of the functional form

$$I(r) = I_e \exp \left[ -b_n \left( \left( \frac{r}{R_h} \right)^{1/n} - 1 \right) \right], \quad (1)$$

to the light profile of each galaxy. The Sérsic index ( $n$ ) is allowed to vary between  $n = 0.2$  and 8 and  $R_h$  defines the galaxy’s stellar half-light radius. The Sérsic models are convolved with the PSF of the broad-band image, derived from stacking unsaturated stars in the frame. We show examples of the imaging, model, and residuals for a sample of galaxies in Appendix B, as well the best quality image available for every KGES galaxy in Appendix

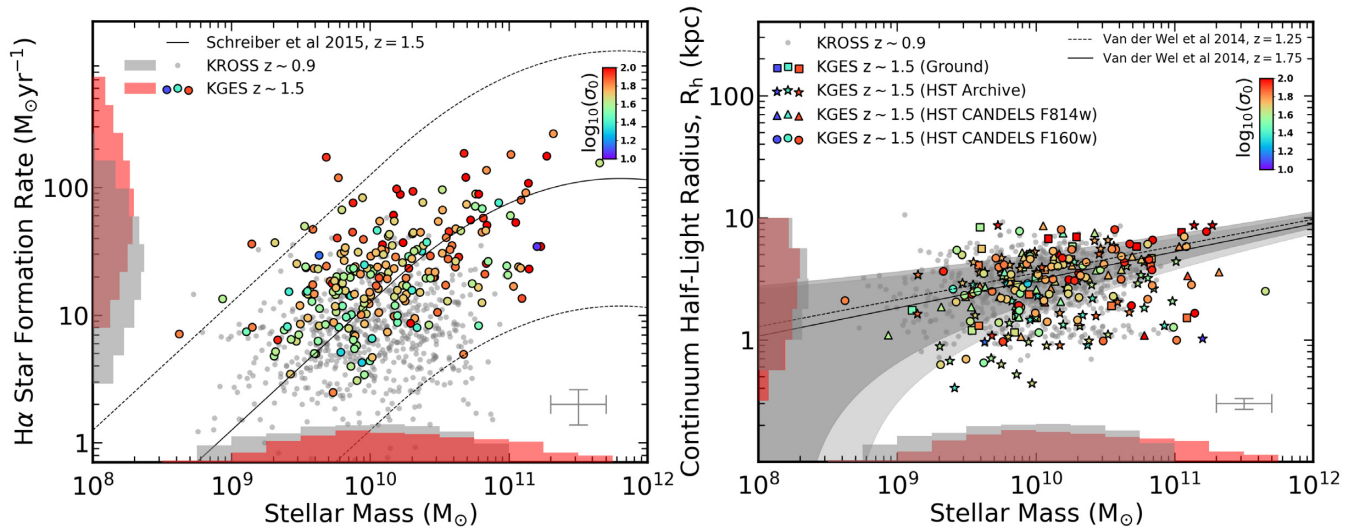


**Figure 2.** *Left-hand panel:* The extinction-corrected  $H\alpha$  star formation rate for the KGES sample as a function of stellar mass as derived from SED fitting using MAGPHYS (da Cunha, Charlot & Elbaz 2008). The KROSS  $z \sim 0.9$  sample is shown as grey points in the background. The Schreiber et al. (2015)  $z = 1.5$  star formation rate stellar mass tracks, converted to a Chabrier IMF, are shown as well as factor 10 above and below the model track. *Right-hand panel:* Stellar continuum half-light radii, derived from GALFIT, as a function of stellar mass. KROSS  $z \sim 0.9$  sample shown as grey points in the background. Ground ( $H$ ,  $K$ ) imaging (squares), non-CANDELS  $HST$  imaging (stars), CANDELS  $HST$  F814W imaging (triangles) and, CANDELS  $HST$  F160W imaging (circles). The dashed and solid lines indicate the mass–size relation for star-forming galaxies at  $z = 1.25$  and  $z = 1.75$  respectively, as derived by van der Wel et al. (2014), with the shaded region indicating the uncertainty on the relations. The median uncertainty on stellar mass, star formation rate, and stellar continuum size are shown by the grey bars in the lower right corner of each panel and the distribution of velocity dispersion within the sample is shown by the colour bar. In both panels we show histograms of each observable for both KROSS and KGES surveys. The figure indicates that the star formation rates and stellar continuum sizes of the KGES galaxies are ‘typical’ of star-forming galaxies at  $z \sim 1.5$ .

**Table 1.** The broad-band imaging available for KGES galaxies that lie in the COSMOS, UDS, and ECDFS fields. Survey, wavelength band, number of galaxies, PSF FWHM, and reference paper/programme ID are given. (CANDELS = The Cosmic Assembly Near-infrared Deep Extragalactic Legacy Survey; COSMOS = Cosmic Evolution Survey; UKIDSS = UKIRT Infrared Deep Sky Survey; TENIS = Taiwan ECDFS Near-Infrared Survey; UVISTA = Ultra Deep Survey near-infrared survey with VISTA telescope; † = Ground-based imaging).

Survey	Band	No. Gal.	PSF FWHM (arcsec)	Reference/Programme ID
CANDELS	F435W, F606W, F814W F105W, F125W, F160W	112	0.22	Koekemoer et al. (2011), Grogin et al. (2011)
CANDELS	F435W, F606W, F814W	50	0.11	Koekemoer et al. (2011), Grogin et al. (2011)
$HST$ Archive	F140W	3	0.22	$HST$ ID: 13793
$HST$ Archive	F125W	3	0.22	$HST$ ID: 15115
COSMOS	F814W	88	0.11	Koekemoer et al. (2007), Massey et al. (2010)
†COSMOS UVISTA DR3	$H$	3	0.76	McCracken et al. (2012)
†UDS UKIDSS DR10	$K$	22	0.77	Lawrence et al. (2007)
†ECDFS TENIS	$K$	7	0.91	Hsieh et al. (2012)

A. For the galaxies with  $HST$  CANDELS F160W coverage, we make a direct comparison of Sérsic index ( $n$ ), half-light radius ( $R_h$ ), and semimajor axis (PA) to van der Wel et al. (2012) who derived the structural properties of galaxies in the CANDELS survey up to  $z = 3$  also using GALFIT. We find median ratios of  $\langle n_{GF}/n_{VW} \rangle = 1.06 \pm 0.01$ ,  $\langle R_{hGF}/R_{hVW} \rangle = 1.00 \pm 0.01$ , and  $\langle PA_{GF}/PA_{VW} \rangle = 1.00 \pm 0.01$ , where the subscript VW denotes van der Wel et al. (2012) measurements and GF denotes our measurement using GALFIT. This indicates that we can accurately recover the structural properties of  $z \sim 1.5$  galaxies using the GALFIT software.

To ensure the measure of a galaxy’s stellar continuum half-light radius is robust and unaffected by recent star formation, we need to measure the morphology of the galaxy in the longest wavelength band. To calibrate the structural properties of galaxies without  $HST$  CANDELS F160W coverage, we use GALFIT to fit Sérsic profiles

in every wavelength band that is available for each galaxy. We use the median ratios of half-light radius, Sérsic index, and semimajor axis in that band to the F160W wavelength band for galaxies with multiwavelength imaging, to ‘correct’ the structural properties to F160W measurements. At  $z = 1.5$   $HST$  F160W filters correspond to  $R$ -band (640nm) while the  $HST$  F814W samples the  $U$ -band (325nm) emission. To ensure the calibration of Sérsic index is valid for galaxies of varying F814W–F160W colour ( $m_{F160W} - m_{F814W}$ ), e.g. galaxies with more diverse stellar populations, we explore correlation between the Sérsic index ratio  $n_{F160W}/n_{F814W}$  and  $m_{F160W} - m_{F814W}$  colour. We fit a linear function of the form

$$\frac{n_{F160W}}{n_{F814W}} = \alpha(m_{F160W} - m_{F814W}) + \beta, \quad (2)$$

finding  $\alpha = -0.47$  and  $\beta = 0.64$ . On average, the ratio of Sérsic index measured in F814W to F160W is  $\langle n_{F160W}/n_{F814W} \rangle = 1.54 \pm$

0.08 and this increases for galaxies with bluer colours. We apply this variable calibration factor to the galaxies with *HST* F814W imaging. The median Sérsic index of KGES galaxies is  $\langle n \rangle = 1.37 \pm 0.12$ , indicating their stellar light distributions are very similar to that of an exponential disc ( $n = 1$ ).

We also correct the stellar continuum half-light radii measured from F814W imaging, to equivalent F160W measurements, following a similar procedure and deriving a fixed correction factor of  $\langle R_{h, F160W} / R_{h, F814W} \rangle = 0.90 \pm 0.02$ . This indicates that, on average, the stellar continuum sizes measured from F814W band imaging are 10 per cent larger than that measured from F160W band imaging. We derive a median intrinsic  $R_h$  of the galaxies in our sample to be  $\langle R_h \rangle = 0.31 \pm 0.02$  ( $2.60 \pm 0.15$  kpc at  $z = 1.5$ ). In Fig. 2, we show the distribution of half-light radius ( $R_h$ ), derived from a variety of imaging (Table 1) as a function of stellar mass for all 288 KGES galaxies. We show tracks of the stellar mass–stellar continuum size relation from van der Wel et al. (2014) for star-forming galaxies at  $z = 1.25$  and  $z = 1.75$  with the shaded region indicating the uncertainty on the relations. The main-sequence galaxy population, in the redshift range  $z = 1.25$ – $1.75$ , with a median stellar mass of  $\log(M_*/[M_\odot]) = 10.25$ , has stellar continuum size 18–64th percentile range of  $\langle R_h \rangle = 1.32$ – $5.5$  kpc (van der Wel et al. 2014). The median size of the KGES galaxies lies within this range and from Fig. 2 we can see that the galaxies in the KGES survey have stellar continuum sizes that are typical of the star-forming population at  $z = 1.5$ .

To place the KGES sample in context of other high-redshift integral field studies of star-forming galaxies, we also show the stellar continuum size distribution of the KROSS survey as a function of stellar mass in Fig. 2. The distribution of sizes in the two surveys is very similar with KROSS having a slightly larger median size of  $\langle R_h \rangle = 0.36 \pm 0.01$  ( $2.80 \pm 0.07$  kpc at  $z = 0.9$ ).

### 3.2.2 Inclination and axis ratios

In Section 3.3, we will measure the rotational velocities of the galaxies in the sample. To correct the dynamics for line-of-sight inclination effects we derive the inclination for each galaxy in the sample. For galaxies that are disc-like, the inclination angle can be calculated using

$$\cos^2(\theta_{\text{inc}}) = \frac{(b/a)^2 - q_0^2}{1 - q_0^2}, \quad (3)$$

where  $\theta_{\text{inc}} = 0$  represents a face-on galaxy (e.g. Tully & Fisher 1977). The value of  $q_0$ , which represents the edge-on axial ratio, depends on the galaxy type, but is typically in the range  $q_0 = 0.13$ – $0.20$  for rotationally supported galaxies at  $z \sim 0$  (e.g. Weijmans & MaNGA Team 2016). We adopt  $q_0 = 0.2$  as this is appropriate for a thick disc (e.g. Guthrie 1992; Law et al. 2012b; Weijmans et al. 2014) and to be consistent with other high-redshift integral field surveys (e.g. KROSS, Harrison et al. 2017; KMOS3D, Wisnioski et al. 2015). The medium axis-ratio of KGES galaxies, derived from the GALFIT modelling, is  $\langle b/a \rangle = 0.60 \pm 0.02$  which equates to a medium inclination of  $\langle \theta_{\text{inc}} \rangle = 55^\circ \pm 2^\circ$ . This corresponds to a medium line-of-sight velocity correction of  $\sim 30$  per cent. To measure the reliability of the axial ratio measurements from GALFIT for the KGES galaxies, we generate 1000 mock galaxies with a distribution of half-light radii, Sérsic index,  $K$ -band magnitude and axis ratios that reflects the KGES sample. We use GALFIT to measure the intrinsic axial ratio of the model galaxies and derive a median ratio of  $\langle b_{\text{int}}/b_{\text{GALFIT}} \rangle = 1.00 \pm 0.01$  with a scatter of 0.40.

We note however that GALFIT performs poorly for very faint small galaxies that have low signal to noise. The median axial ratio is in agreement with the results of Law et al. (2012a) who use the rest-frame *HST* optical images for  $z \approx 1.5$ – $3.6$  star-forming galaxies and find a peak axial ratio of  $\langle b/a \rangle \sim 0.6$ .

### 3.2.3 Concentration, Asymmetry, and Clumpiness (CAS)

In Section 4.3, we will correlate the dynamics of the galaxies with their morphologies, so to provide a non-parametric model-independent measurement of galaxies rest-frame optical morphology, we next derive the concentration, asymmetry, and clumpiness (CAS; Abraham et al. 1996; Conselice 2003, 2014) of the continuum stellar light distribution of the galaxies in our sample. As shown by Conselice (2003), due to their non-parametric nature, the CAS parameters of star-forming galaxies can be reliably measured out to high redshift and they capture the major features of the stellar structure in a galaxy without assuming an underlying form, e.g. Sérsic fitting in the case of GALFIT. We note due to the complex, non-linear, nature of converting non-parametric measures of a galaxies morphology between different wavelength bands, we do not measure the CAS parameters for galaxies without *HST* imaging. For galaxies with *HST* imaging, we derive the CAS parameters in F814W *I*-band imaging as this maximizes the sample size and allows an accurate comparison to the KROSS survey which predominately has *HST* F814W *I*-band imaging.

The concentration ( $C$ ) of a galaxy is a measure of how much light is in the central regions of the galaxy compared to the outskirts and is calculated from

$$C = 5 \times \log_{10} \left( \frac{r_{\text{outer}}}{r_{\text{inner}}} \right), \quad (4)$$

where  $r_{\text{outer}}$  is the radius which contains 80 per cent of the light within an aperture of semimajor axis  $3R_h$ ,  $r_{\text{inner}}$  is the radius which contains 20 per cent of the light within the same aperture. A higher value of concentration indicates a larger fraction of the galaxies' light originates from the central regions. The median concentration for our sample is  $\langle C \rangle = 2.36 \pm 0.34$ . For comparison we also measured the concentration of galaxies in the KROSS  $z = 0.9$  sample with *HST* imaging (178 galaxies), finding  $\langle C \rangle = 2.4 \pm 0.27$  which implies, on average, the stellar light profiles of  $z = 0.9$  star-forming galaxies are more concentrated than  $z = 1.5$  galaxies. Conselice (2003) identified that in a sample of 250  $z \sim 0$  galaxies, late-type discs have a median concentration of  $\langle C \rangle = 3.1 \pm 0.4$ , while local early-type galaxies have much higher concentration of  $\langle C \rangle = 3.9 \pm 0.5$ . Local irregular galaxies were established to have a  $\langle C \rangle = 2.9 \pm 0.3$  indicating high-redshift galaxies have stellar light distributions with concentrations similar to local irregular galaxies.

The asymmetry ( $A$ ) of a galaxy reflects the fraction of light originating from non-symmetric components, where a perfectly symmetric galaxy would have  $A = 0$  and a maximally asymmetric galaxy would have  $A = 1$ . The asymmetry estimator of a galaxy is defined as

$$A = \min \left( \frac{\sum |I_0 - I_{180}|}{\sum |I_0|} \right) - \min \left( \frac{\sum |B_0 - B_{180}|}{\sum |I_0|} \right), \quad (5)$$

where  $I_0$  represents the original galaxy image and  $I_{180}$  is the image rotated by  $180^\circ$  about its centre.  $B_0$  and  $B_{180}$  represent a region of sky of equal size nearby to the galaxy (Conselice 2014). The true asymmetry of the galaxy is measured by minimizing over the centre of symmetry and is calculated within an ellipse of semimajor axis  $3R_h$ , where  $R_h$  is convolved with the PSF of the image, with an axial



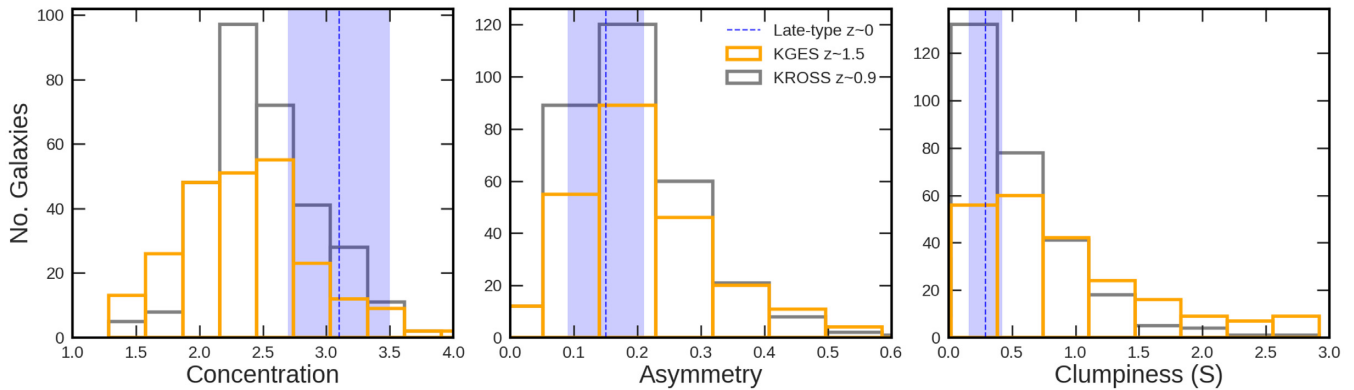


**Figure 3.** Histograms of the concentration, asymmetry, and clumpiness of the KGES  $z \sim 1.5$  galaxies (orange) measured from *HST* F814W imaging. We also show the distribution of the KROSS  $z \sim 0.9$  survey (Harrison et al. 2017) with *HST* F814W imaging (grey) as well as the median values and scatter (blue line and shaded region) for a sample of late-type  $z = 0$  galaxies from Conselice (2003) who used *R*-band imaging. The KGES galaxies are comparable in concentration and asymmetry to KROSS, while being clumpier on average. The  $z = 0$  sample is more concentrated and less clumpy than KGES while having similar asymmetry.

ratio and position angle matching that derived from Sérsic fitting in Section 3.2.1.

Since the asymmetry is a function of signal to noise (Conselice 2003), we assess the reliability of asymmetry measurements by creating 100 mock galaxies with Sérsic index  $n = 0.5$ – $2$ ,  $R_h = 0.1$ – $1.0$  arcsec, and a signal-to-noise distribution similar to our data. The asymmetry in each galaxy is calculated first within an ellipse of semimajor axis  $3R_h$  ( $A_{\text{Mask}}$ ) and compared to the true asymmetry of each galaxy ( $A_{\text{True}}$ ), derived from the full extent of the galaxy with infinite signal to noise. We then compare  $A_{\text{True}}$  to the asymmetry within an ellipse of semimajor axis  $3R_h$  for galaxies that have signal to noise of 10 ( $A_{10}$ ). We find a median ratio of  $\langle A_{\text{True}} / A_{\text{Mask}} \rangle = 1.01 \pm 0.03$  while  $\langle A_{\text{True}} / A_{10} \rangle = 1.05 \pm 0.01$ . This indicates that on average the asymmetry of the galaxies, although slightly underestimated, are accurate to a few per cent when calculated within an ellipse of semimajor axis  $3R_h$ , even in our lowest signal to noise sources.

For the KGES galaxies we derive a median asymmetry of  $\langle A \rangle = 0.19 \pm 0.05$  with a range from  $A = 0.01$ – $0.85$ . In a study of  $z \sim 0$  galaxies by Conselice (2003), late-type galaxies have  $\langle A \rangle = 0.15 \pm 0.06$ , while early-types have  $\langle A \rangle = 0.07 \pm 0.04$  and irregular galaxies have  $\langle A \rangle = 0.17 \pm 0.10$ . The galaxies in the KGES survey have asymmetries equivalent to those of local late-type and irregular galaxies. In Section 4.2, we will also compare the dynamics and morphology of the KROSS sample to the KGES galaxies. We therefore derive the asymmetry of the KROSS galaxies, finding  $\langle A \rangle = 0.16 \pm 0.06$ .

We can parametrize the fraction of light originating from clumpy distributions in a galaxy using the clumpiness parameter,  $S$ , which is defined as

$$S = 10 \times \left[ \left( \frac{\sum (I_{x,y} - I_{x,y}^\sigma)}{\sum I_{x,y}} \right) - \left( \frac{\sum B_{x,y} - B_{x,y}^\sigma}{\sum I_{x,y}} \right) \right], \quad (6)$$

where  $I_{x,y}$  is the original image and  $I_{x,y}^\sigma$  is a smoothed image. The degree of smoothing, as defined by Conselice (2003), is relative to the size of the galaxy and is quantified by  $\sigma = 0.2 \times 3R_h$ , where  $\sigma$  is the standard deviation of the Gaussian kernel. The residual map generated from subtracting the smoothed image from the original contains only high-frequency structures in the galaxy. The central region of the galaxy is masked out in this process as it is often unresolved.

The same method is applied to an arbitrary region of background away from the galaxy ( $B_{x,y}$ ,  $B_{x,y}^\sigma$ ) to remove the inherent clumpiness of the noise in the image. We derive the clumpiness for the galaxies in the KGES sample finding a median clumpiness of  $\langle S \rangle = 0.37 \pm 0.14$  with a range from  $S = 0.01$ – $5.3$ . In comparison to the local Universe, Conselice (2003) identified that  $z \sim 0$  late-type galaxies have  $\langle S \rangle = 0.29 \pm 0.13$ , early-type galaxies have  $\langle S \rangle = 0.08 \pm 0.08$ , and irregular galaxies have  $\langle S \rangle = 0.40 \pm 0.20$ . The clumpiness distribution of KGES galaxies aligns with that of late-type local disc galaxies, although we note that a larger will reduce the clumpiness measured in a galaxy. As a comparison sample we also derive the clumpiness for the galaxies in the KROSS sample, finding a median value of  $\langle S \rangle = 0.37 \pm 0.10$ .

Law et al. (2012a) established that a typical main-sequence star-forming galaxy in the redshift range  $z = 1.5$ – $3.6$  is well described by a Sérsic profile of index  $n \sim 1$ , concentration index  $C \sim 3$  and asymmetry index  $A \sim 0.25$ . The galaxies in the KGES sample have Sérsic and CAS parameters that align with typical star-forming galaxies at  $z = 1.5$ . We show the distribution of concentration, asymmetry, and clumpiness of the KGES  $z \sim 1.5$  galaxies in comparison to the KROSS  $z \sim 0.9$  survey as well as the median values and scatter for a sample of late-type  $z = 0$  galaxies from Conselice (2003) in Fig. 3.

### 3.3 Kinematics

We next turn our attention to the kinematics of the KGES sample. A full description of the emission-line fitting procedure and extraction of kinematic properties is given in Tilely et al. (in preparation). Here, we give a brief overview of the emission-line fitting procedure and then we discuss the rotational velocity and velocity dispersion measurements that enable us to quantify more derived properties of the KGES galaxies.

#### 3.3.1 Emission-line fitting

Briefly, we fit a triple Gaussian profile to the continuum-subtracted  $H\alpha$  ( $\lambda 6562 \text{ \AA}$ ) and  $[\text{N II}]$  ( $\lambda 6548 \text{ \AA}$ ,  $\lambda 6583 \text{ \AA}$ ) emission-line profiles in all 288 KGES galaxies, with the redshift, emission-line width, and emission-line amplitude as free parameters. The three emission lines share a common width and their relative positions are



fixed according to Osterbrock & Ferland (2006). The instrumental broadening of the OH sky lines by KMOS is used to correct for instrumental broadening.

For each galaxy, we fit the emission-line profiles in the integral field observation using an adaptive binning technique. Starting in apertures of  $0.3 \times 0.3$  arcsec (comparable to half the FWHM of the seeing), we impose an  $H\alpha$  signal to noise threshold of  $S/N \geq 5$  on the integrated  $S/N$  of the emission line. If this  $S/N$  is not achieved, we fit to the spectrum over a larger area until either the  $S/N$  threshold is achieved or the binning limit of  $0.7 \times 0.7$  arcsec (comparable to the FWHM of the seeing) is reached. In Fig. 4, we show examples of the spatially resolved  $H\alpha$  intensity, velocity, and velocity dispersion maps for a number of KGES galaxies. The  $H\alpha$  velocity for all KGES galaxies is shown in Appendix A. The galaxies in our sample have predominantly rotationally supported gas kinematics with  $\langle V_{2R_h}/\sigma_0 \rangle = 1.93 \pm 0.21$  where 68 per cent of KGES galaxies have  $v/\sigma > 1$ , within which  $V_{2R_h}$  is the rotation velocity of the galaxy and  $\sigma_0$  is the intrinsic velocity dispersion, as defined in Sections 3.3.2 & 3.3.3. To quantify the misalignment between the kinematic and morphological axis we define the misalignment parameter  $\Psi$  as

$$\sin \Psi = |\sin(\text{PA}_{\text{morph}} - \text{PA}_{\text{kin}})|, \quad (7)$$

where  $\Psi$  is defined between  $0^\circ$  and  $90^\circ$  (Wisnioski et al. 2015). For the KGES sample  $\langle \Psi \rangle = 18.65^\circ \pm 1.98^\circ$  with 66 per cent of KGES galaxies passing the galaxy disc criteria of  $\Psi < 30^\circ$ . This fraction increases to 78 per cent with  $\Psi < 40^\circ$ . This indicates that the KGES galaxies have well-defined velocity gradients that reflect the stellar morphology shown in the first panel of Fig. 4. This indicates that most of the high-redshift galaxies in the KGES sample are predominantly rotation-dominated galaxies with defined rotation axes. The distribution of  $H\alpha$  velocity maps for the full sample in the specific stellar angular momentum stellar mass plane is shown in Fig. 5. We note, however, that some ‘disc’ galaxies in seeing-limited observations have been identified as mergers in higher resolution adaptive optics observations (e.g. Rodrigues et al. 2017; Sweet et al. 2019; Espejo et al., in preparation).

### 3.3.2 Rotation velocities

To measure the correlation between the dynamics of the galaxies in our sample and their rest-frame optical morphologies, we need to parametrize their kinematics. We quantify the dynamics by measuring the asymptotic rotational velocity of each galaxy derived from the spatially resolved  $H\alpha$  velocity maps.

The rotation curve of a galaxy is defined as the velocity profile extracted about the galaxy’s kinematic position angle. For each galaxy, we measure the kinematic position angle by rotating the velocity map in one degree increments about the galaxy’s continuum centre (defined from *HST*). For each step we calculate the velocity gradient along a horizontal ‘slit’ of width equal to half the FWHM of the PSF of the seeing. We define the kinematic position angle as the average of the angle with maximum velocity gradient and the angle of minimum velocity gradient plus  $90^\circ$ . We extract the velocity profile at the kinematic position angle, with the velocity and uncertainty taken as the weighted mean and standard error along pixels perpendicular to the ‘slit’.

We choose this method to derive the rotation profiles of the galaxies in the KGES sample as opposed to forward modelling approaches (e.g. Di Teodoro, Fraternali & Miller 2016) since this reduces the number of assumptions about the galaxy’s dynamical

state. We note, however, in doing so the extracted rotation curves are effected by beam smearing but by following the procedures of Johnson et al. (2018), these effects can be reduced to less than the 10 per cent level.

To minimize the scatter in the velocity profiles and to allow for the possibility of rising, flat or declining rotation curves, we fit each galaxy’s rotation curve with a parametric model. We choose an exponential light profile (see Freeman 1970) since the kinematics, as shown in Fig. 4, indicate the majority of the galaxies are rotationally supported with large-scale ordered rotation. The dynamical model is parametrized as follows:

$$v(r)^2 = \frac{r^2 \pi G \mu_o}{r_D} (I_o(x) K_o(x) - I_1(x) K_1(x)), \quad (8)$$

where  $G$  is the gravitational constant,  $\mu_o$  is the peak mass surface density,  $r_D$  is the disc scale radius, and  $I_n(x) K_n(x)$  are Bessel functions evaluated at  $x = 0.5r/r_D$ . The rotation velocities and best-fitting dynamical models are shown in Fig. 4 for a subsample of KGES galaxies. We do not interpret the model parameters, nor extrapolate the model to large radii, but rather use the model to trace the observed rotational velocity profiles and account for the effect of noise in the outer regions.

Next, we measure the rotational velocity of each galaxy by extracting the velocity from the galaxy’s rotation curve at  $2R_h$  ( $=3.4R_d$  for an exponential disc where  $R_d$  is the light profile scale radius; e.g. Miller et al. 2011). As shown by Romanowsky & Fall (2012), the velocity at  $2R_h$  provides a reliable estimate of a galaxy’s rotation velocity irrespective of its morphology. At  $2R_h$ , the velocity profile of an exponential disc, with a nominal dark matter fraction, begins to flatten and the effects of beam smearing are minimized. It is also crucial for capturing the majority of a galaxy’s angular momentum (e.g. Obreschkow et al. 2015), as we demonstrate in Section 3.4 for the KGES galaxies and allows comparison to other spatially resolved studies of star-forming galaxies (e.g. KMOS<sup>3D</sup>, KROSS, Wisnioski et al. 2015; Harrison et al. 2017).

The extracted velocity, from the dynamical model, is inclination and beam smear corrected following the procedures described in Johnson et al. (2018) with a median correction factor of  $\langle V_{\text{obs}}/V_{\text{int}} \rangle = 1.05 \pm 0.01$ . The median intrinsic rotation velocity of the KGES galaxies is  $\langle V_{2R_h} \rangle = 102 \pm 8 \text{ km s}^{-1}$ , with a 16–84th percentile range of 27–191  $\text{km s}^{-1}$ .

For 50 of the galaxies in the KGES sample, the low  $S/N$  of the  $H\alpha$  emission means we do not spatially resolve the galaxy out to  $2R_h$ . In these galaxies, we extrapolate the dynamical model beyond the last data point to measure the rotation velocity at  $2R_h$ . To understand whether this affects the derived rotation velocity we measure the ratio of the radius of the last data point on the rotation curve to  $2R_h$  and the ratio of the velocity of the last data point to the velocity extracted at  $2R_h$ . For galaxies we do resolve, we identify that  $\langle R_{\text{last}}/2R_h \rangle = 1.6 \pm 0.08$  and  $\langle V_{\text{last}}/V_{2R_h} \rangle = 1.01 \pm 0.03$ , while for the 50 galaxies we do not resolve out to  $2R_h$ ,  $\langle R_{\text{last}}/2R_h \rangle = 0.84 \pm 0.04$  and  $\langle V_{\text{last}}/V_{2R_h} \rangle = 0.97 \pm 0.02$ . This indicates that on average when the  $H\alpha$  rotation curve does not extend out to  $2R_h$ , a 15 per cent extrapolation is required and the extracted velocity at  $2R_h$  is slightly less than that at  $R_{\text{last}}$ .

To put the dynamics of the galaxies in the KGES sample in the context of other high-redshift star-forming galaxy surveys, we make a comparison to the KROSS sample of  $\sim 600$  star-forming galaxies at  $z \sim 0.9$ . Harrison et al. (2017) extract the rotation velocity of the KROSS galaxies at  $2R_h$  and applying the beam smearing corrections derived in Johnson et al. (2018). The KROSS sample has a median intrinsic rotational velocity of  $\langle V_{\text{int}} \rangle = 117 \pm 4 \text{ km s}^{-1}$  with a

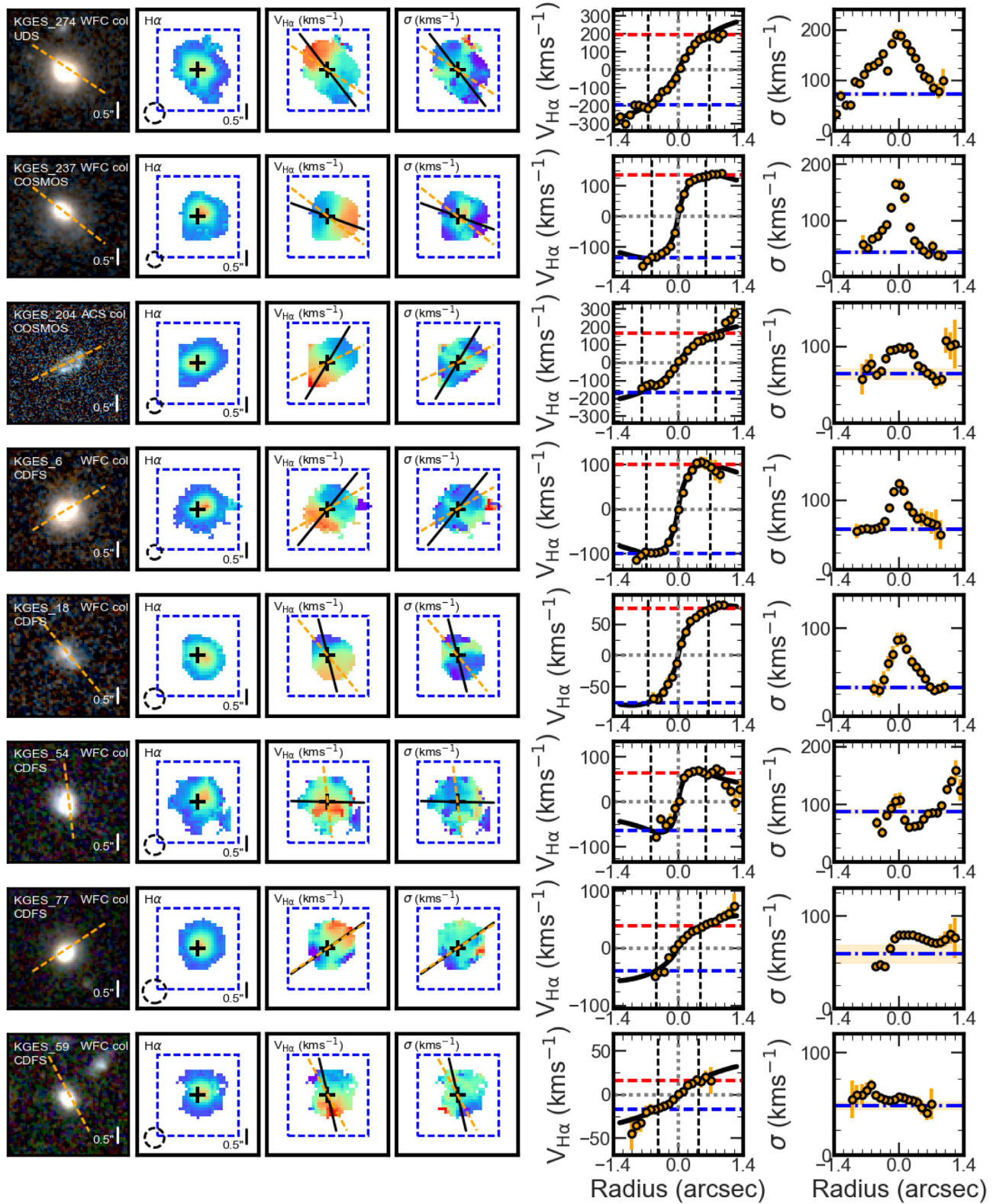


**Figure 4.** Example of spatially resolved galaxies in the KGES sample from each quartile of specific stellar angular momentum. From left to right: broad-band imaging of the galaxy (left), with semimajor axis (PAim; orange dashed line),  $H\alpha$  intensity map, velocity map, and velocity dispersion map, derived from the emission-line fitting with data cube field of view (blue dashed square). Kinematic position angle (PAvel; black solid line) and PAim (orange dashed line) axes are plotted on the rotation and dispersion velocity maps. Rotation curve and dispersion profile extracted about the kinematic position axis (right). The rotation curve shows lines of  $2R_h$  derived from Sérsic fitting, as well as  $V(2R_h)$  (red and blue dashed lines) extracted from the rotation curve fit (black curve). The dispersion profile shows the extracted  $\sigma_{\text{int}}$  (blue dashed line) and  $1\sigma$  region (yellow shaded region).

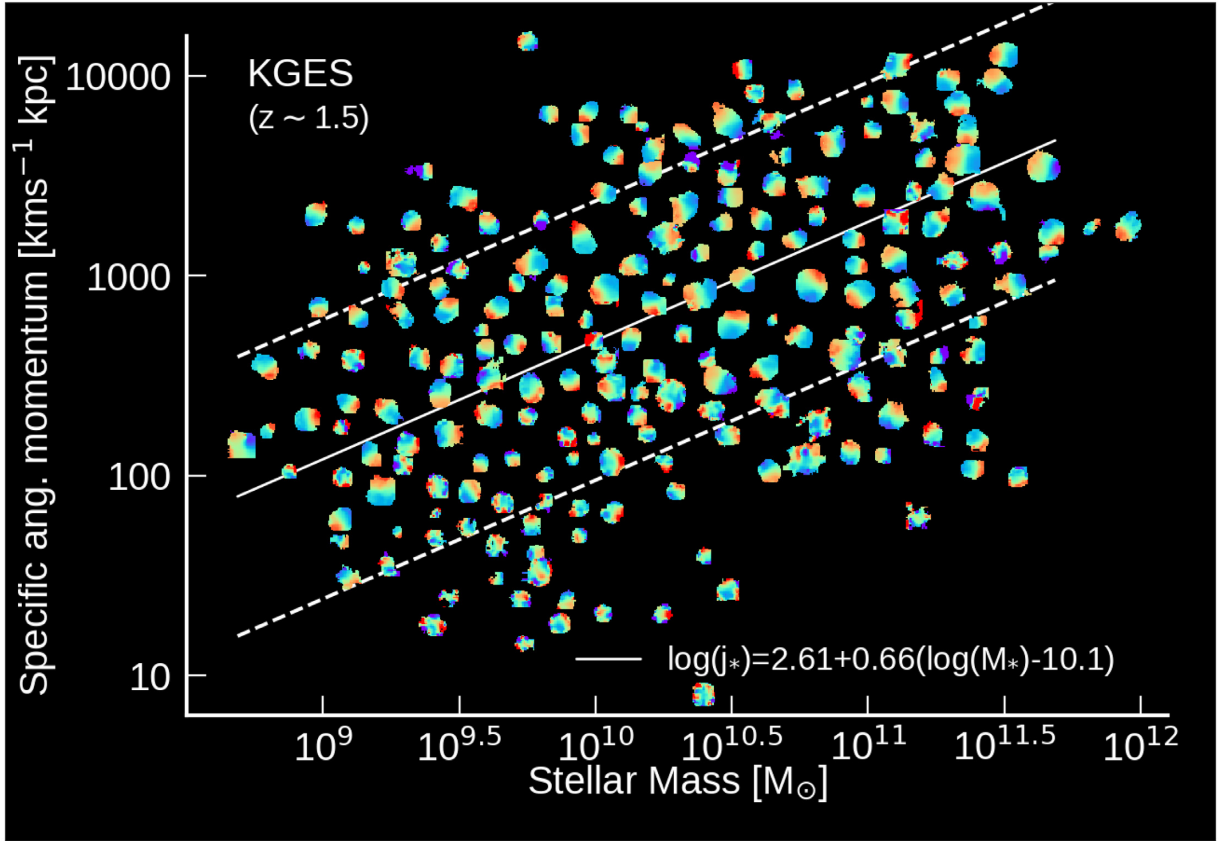


**Figure 5.** The  $H\alpha$  rotational velocity maps of the KGES galaxies with  $H\alpha$  signal to noise greater than 5, displayed in the specific stellar angular momentum stellar mass plane, offset to minimize overlap. The white solid line is a fit to the KGES data of the form  $\log_{10}(j_*) = \alpha + \beta(\log_{10}(M_*/M_\odot) - 10.10)$ , with the slope fixed to  $\beta = 0.66$  and a derived intercept of  $\alpha = 2.61$ . The white dashed lines are a factor of 10 above and below the fit. Low stellar mass, low angular momentum galaxies have smaller stellar continuum sizes and thus have a smaller extent of nebula emission compared to galaxies of higher stellar mass and higher angular momentum.

16–84th percentile range of  $46\text{--}205\text{ km s}^{-1}$ . In the KROSS sample, galaxies have higher rotation velocities than the KGES galaxies at  $z \sim 1.5$ .

The distribution of stellar mass in both the KROSS and KGES surveys is very similar with both samples having a median stellar mass of  $\log(M_*/M_\odot) = 10.0 \pm 0.2$ . The origin of the evolution in rotation velocities may be driven by the biases in the selection function of the two surveys or by an evolution in pressure support within the galaxies (e.g. [Tiley et al. 2019](#), [Übler et al. 2019](#)). Establishing the exact cause is beyond the scope of this paper, but will be discussed in [Tiley et al. \(in preparation\)](#).

### 3.3.3 Velocity dispersion

To analyse the connection between a galaxy’s rest-frame optical morphology, dynamics and the balance between rotational and pressure support, we need to measure the intrinsic velocity dispersion (disc thickness) within each galaxy. We assume that a galaxy’s intrinsic dispersion profile is flat and that the velocity dispersion is a good proxy for the turbulence (non-circular motions) within a galaxy.

We attempt to measure the dispersion profile of each galaxy out to  $1.3R_h$ . We choose  $1.3R_h$  as opposed to  $2R_h$ , as more galaxies have kinematic information at  $1.3R_h$  and we identify that the derived velocity dispersion is very similar with  $\langle \sigma_{1.3R_h} / \sigma_{2R_h} \rangle = 1.00 \pm 0.07$ .

If the spatially resolved kinematics of the galaxy do not extend out to  $1.3R_h$ , we measure the median dispersion from the velocity dispersion map of the galaxy, examples of which are shown in [Fig. 4](#). The extracted values are then corrected for beam smearing following the methods described in [Johnson et al. \(2018\)](#), which use model-based corrections to derive an intrinsic velocity dispersion for each galaxy.

For the sample of 235 resolved galaxies the median line-of-sight velocity dispersion is  $\langle \sigma_0 \rangle = 52 \pm 2\text{ km s}^{-1}$ , with a 16–84th percentile range of  $37\text{--}72\text{ km s}^{-1}$ . In comparison, the KROSS sample of galaxies at  $z \sim 0.9$  has a median velocity dispersion of  $\langle \sigma_0 \rangle = 44 \pm 1\text{ km s}^{-1}$ . [Übler et al. \(2019\)](#) established that star-forming galaxies at  $z = 2.3$  have an ionized gas velocity dispersion of  $\langle \sigma_0 \rangle = 45\text{ km s}^{-1}$ , while for galaxies at  $z = 0.6$ ,  $\langle \sigma_0 \rangle = 30\text{ km s}^{-1}$ . This indicates that main-sequence star-forming galaxies at  $z \sim 1.5$  have 20 per cent higher levels of turbulence compared to  $z \sim 0.9$  main-sequence galaxies while having comparable levels of dispersion to higher redshift galaxies. This is in agreement with the findings of previous high-redshift integral field studies (e.g. [Wisnioski et al. 2015](#); [Johnson et al. 2018](#); [Übler et al. 2019](#), [Tiley et al., in preparation](#)).

In [Fig. 6](#), we show the velocity dispersions of both the KGES and KROSS galaxies as a function of their  $H\alpha$  star formation rate, with the KGES galaxies coloured by their stellar mass. Galaxies of higher star formation rate have higher stellar mass, as reflected in the main-sequence in [Fig. 2](#). We also show the feedback-driven



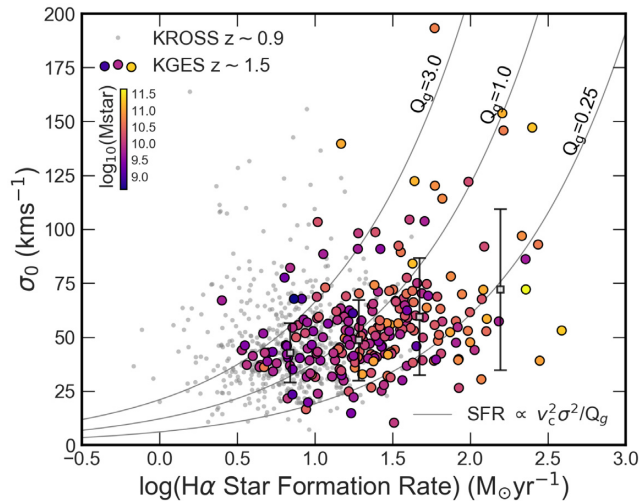


**Figure 6.** Velocity dispersion ( $\sigma_0$ ) as a function of the H $\alpha$  star formation rate for KGES (coloured points) and KROSS (grey points) galaxies. KGES galaxies are coloured by their stellar mass ( $M_*$ ) with the median and standard deviation of velocity dispersion in bins of H $\alpha$  star formation rate shown by the square points. Galaxies of a higher star formation rate have higher stellar mass (Fig. 2). We show the feedback-driven turbulence model from Krumholz & Burkhardt (2016) for the relation between star formation rate and velocity dispersion, parametrized as  $\text{SFR} \propto v_c^2 \sigma^2 / Q_g$ , for different Toomre  $Q_g$  values, evaluated at the median rotational velocity of the KGES sample,  $\langle V_{2R_h} \rangle = 102 \pm 8 \text{ km s}^{-1}$ . The KGES galaxies occupy similar  $\sigma_0$ –SFR parameter space as galaxies with  $Q_g = 0.25$ –3.0.

turbulence model from Krumholz & Burkhardt (2016) for the relation between star formation rate and velocity dispersion, parametrized as  $\text{SFR} \propto v_c^2 \sigma^2 / Q_g$ , for different Toomre  $Q_g$  values, evaluated at the median rotational velocity of the KGES sample,  $\langle V_{2R_h} \rangle = 102 \pm 8 \text{ km s}^{-1}$ . The KGES galaxies occupy similar  $\sigma_0$ –SFR parameter space as galaxies with  $Q_g = 0.25$ –3.0.

To quantify the kinematic state of the galaxies in our sample we take the ratio of rotation velocity ( $V_{2R_h}$ ) to velocity dispersion ( $\sigma_0$ ). Galaxies with dynamics that are dominated by rotation will have  $V_{2R_h}/\sigma_0 > 1$  while those with kinematics driven by turbulent pressure-support have  $V_{2R_h}/\sigma_0 < 1$ . The median ratio of rotation velocity to velocity dispersion in the KGES sample is  $\langle V_{2R_h}/\sigma_0 \rangle = 1.93 \pm 0.21$  with a 16–84th percentile range of  $V_{2R_h}/\sigma_0 = 0.52$ –3.89. This is within  $1\sigma$  of  $z \sim 0.9$  galaxies in the KROSS survey, which have  $\langle V_{2R_h}/\sigma_0 \rangle = 2.5 \pm 1.4$  (Harrison et al. 2017), but considerably higher than that Turner et al. (2017) derived for star-forming galaxies at  $z \sim 3.5$  in the KMOS Deep Survey, with  $\langle V_{2R_h}/\sigma_0 \rangle = 0.97 \pm 0.14$ . This indicates that the kinematics of the galaxies in our sample are, on average, rotation dominated, and representative of the main-sequence population at  $z \sim 1.5$ .

### 3.4 Angular momentum

In this section, we measure the specific stellar angular momentum ( $j_*$ ) of each galaxy in the KGES sample. We first confirm that the angular momentum of a disc galaxy can be calculated from the integral of the galaxy’s one-dimensional rotation and stellar mass profiles as well as from the approximation of asymptotic rotation speed and stellar disc size, as first proposed by Romanowsky & Fall (2012) (see also Obreschkow & Glazebrook 2014). In the following sections, we then explore the correlation of specific stellar angular momentum with stellar mass and analyse the morphological and

dynamical properties of the galaxies that scatter about the median  $j_*$ – $M_*$  relation.

#### 3.4.1 Asymptotic and integrated specific stellar angular momentum

The specific stellar angular momentum is one of most fundamental properties of a galaxy. It combines the rotation velocity profile and the stellar disc size of the galaxy while removing the inherent scaling with stellar mass (Peebles 1969; Fall & Efstathiou 1980; Fall 1983).

The specific stellar angular momentum is given by

$$\vec{j}_* = \frac{\vec{J}_*}{M_*} = \frac{\int \mathbf{r} \times \bar{\mathbf{v}}(r) \rho_*(r) d^3 \mathbf{r}}{\int \rho_*(r) d^3 \mathbf{r}}, \quad (9)$$

where  $\mathbf{r}$  and  $\bar{\mathbf{v}}$  are the position and mean-velocity vectors (with respect to the centre of mass of the galaxy) and  $\rho(r)$  is the three-dimensional density of the stars (Romanowsky & Fall 2012). To derive the specific angular momentum from observations, we can use two different approaches which require a number of approximations. We derive the integrated specific stellar angular momentum ( $j_*$ ) of a galaxy by integrating the galaxies rotation velocity and surface brightness profiles. Secondly, we derive the asymptotic specific stellar angular momentum ( $\tilde{j}_*$ ), using the parametrized morphology (e.g. Sérsic index, stellar continuum size) and asymptotic rotation velocity of the galaxy. In this section, we measure both  $j_*$  and  $\tilde{j}_*$  for the galaxies in KGES sample to compare both methods and explore their correlations with galaxy morphology. In doing so we are assuming that the gas kinematics are good tracers of the stellar angular momentum, which may introduce a small systematic of  $\approx 0.1$  dex when comparing directly to stellar measurements, based on low-redshift studies (e.g. Cortese et al. 2014, 2016).

First, we calculate the integrated specific stellar angular momentum ( $j_*$ ) of the KGES galaxies. If the dynamics of the stars and gas in the galaxies are comprised of only circular orbits, the normal of the specific stellar angular momentum relative to the centre of gravity can be written as

$$j_* = \left| \frac{J_*}{M_*} \right| = \frac{\int_0^\infty \Sigma(r) v(r) r^2 dr}{\int_0^\infty \Sigma(r) r dr}, \quad (10)$$

where  $\Sigma(r)$  is the azimuthally averaged surface mass density of the stellar component of the galaxy and  $v(r)$  is the rotation profile. To evaluate this formula for galaxies in the KGES sample, we use the near-infrared surface brightness profiles  $I(r)$  as a proxy for the surface mass density, under the assumption that mass follows light. As discussed in Section 3.2 the majority of the galaxies in the sample have *HST* CANDELS imaging in the near-infrared, i.e. rest-frame optical, which traces the old stellar population.

To derive a galaxies surface mass density profile, we calculate the intrinsic surface brightness profile of the galaxy from the *HST* image and then convolve it with the KMOS PSF. Integrating this with the rotation velocity profile, measured in Section 3.3, we derive a specific stellar angular momentum profile for each galaxy. We then derive an estimate of the total specific angular momentum of each galaxy ( $j_*$ ) by extracting the specific stellar angular momentum at  $2 \times$  half-stellar mass radius ( $\sim 3.4 R_d$ ) from the angular momentum profile.

The second approach to measuring a galaxy’s integrated specific stellar angular momentum ( $j_*$ ) is to derive the galaxy’s asymptotic specific stellar angular momentum ( $\tilde{j}_*$ ). Romanowsky & Fall (2012) showed that the total angular momentum, for galaxies of varying morphological type, can be approximated by a combination of



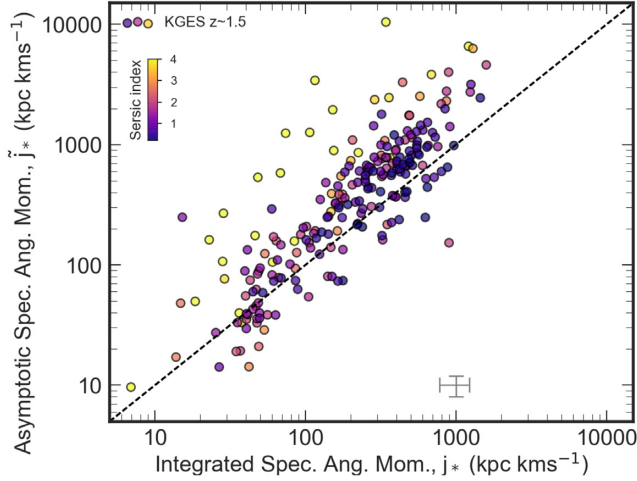


**Figure 7.** The asymptotic specific stellar angular momentum ( $\tilde{j}_*$ ) as a function of the integrated specific angular momentum ( $j_*$ ) evaluated at  $2 \times$  half-stellar mass radius, for the KGES sample. The black dashed line indicates a one-to-one relation. The colourbar indicates the Sérsic index of the galaxy. The scatter below the line is a consequence of deconvolution with a broad-band PSF and convolution with the KMOS PSF. Scatter above the line is driven by galaxies of a higher Sérsic index in which the integrated specific angular momentum at  $2 \times$  half-stellar mass radius is an underestimate of the total angular momentum in the galaxy.

asymptotic rotation speed, stellar disc size, and Sérsic index,

$$\tilde{j}_* = k_n C_i v_s R_h, \quad (11)$$

where  $v_s$  is the rotation velocity at  $2 \times$  the half-light radius ( $R_h$ ),  $C_i$  is the correction factor for inclination, assumed to be  $\sin^{-1}(\theta_{\text{inc}})$  (see appendix A of Romanowsky & Fall 2012) and  $k_n$  is a numerical coefficient that depends on the Sérsic index ( $n$ ) of the galaxy and is approximated as

$$k_n = 1.15 + 0.029n + 0.062n^2. \quad (12)$$

This approximation is valid if the surface brightness profile of the galaxy can be well described by a single component Sérsic profile parametrized by a half-light radius ( $R_h$ ) and Sérsic index ( $n$ ). Thus  $\Sigma(r) \propto \exp(-r/R)$  and assuming the exponential disc is rotating at a constant rotation velocity ( $v_s$ ),

$$j_*(r) = \left[ 2 + \frac{(r/R)^2}{1 + r/R - \exp(r/R)} \right] R_h v_s. \quad (13)$$

For further details on the potential limitations of this approach we refer the reader to Obreschkow & Glazebrook (2014).

To compare the two methods, in Fig. 7, we plot the asymptotic specific stellar angular momentum ( $\tilde{j}_*$ ) as a function of the integrated specific angular momentum ( $j_*$ ). Galaxies with high Sérsic index ( $n > 2$ ) appear to scatter above the line, with the asymptotic specific angular momentum being overestimated, while galaxies with  $n \sim 1$ , scatter about the line.

To understand the source of the scatter within this plane we measure both the asymptotic and integrated specific angular momentum for 1000 mock galaxies with  $\log(M_*/[M_\odot]) = 9-10.5$ , Sérsic index  $n = 0.5-8$ , and half stellar mass radii in the range  $R_h = 0.1-2.0$  arcsec. A tight correlation between  $\tilde{j}_*$  and  $j_*$  is identified for galaxies with  $n = 0.5-2$  of all stellar masses and continuum sizes, with  $\langle \tilde{j}_*/j_* \rangle = 0.88 \pm 0.03$ , when the PSF of both the mock broad-band and integral field data is  $\approx 0$  arcsec. The integrated specific stellar angular momentum ( $j_*$ ) overestimates the angular momentum of

galaxies, when a non-zero PSF is used. The inner regions of the angular momentum profile of the galaxy are not resolved in the convolution process, especially when the PSF is comparable to the galaxies' stellar continuum size.

For mock galaxies with Sérsic index  $n = 2-8$ ,  $\langle \tilde{j}_*/j_* \rangle = 2.88 \pm 0.94$  with the integrated specific stellar angular momentum being underestimated in galaxies of a higher Sérsic index. Romanowsky & Fall (2012) comment that the reliability of  $\tilde{j}_* \approx j_*$  depends systematically on the density profile, where for galaxies with  $n = 2, 4$ , and  $6$ ,  $\tilde{j}_* = j_*$  at  $R \sim 2, 4.5$ , and  $10R_h$ , highlighting that the extended envelopes of higher Sérsic index galaxies contribute more to  $j_*$ .

For the remainder of the analysis on the KGES sample we therefore adopt  $\tilde{j}_*$  (equation 11) as the estimate of the total specific stellar angular momentum in the galaxies which is expected to recover the total angular momentum of a galaxy to within four per cent (Romanowsky & Fall 2012).

### 3.5 Summary of morphological and dynamical properties

We detected H $\alpha$  and [N II] emission in 243 of our targets (84 per cent of the sample) and showed that they are representative of main-sequence star-forming galaxies at  $z \sim 1.5$  (Section 3.1). We parametrized their rest-frame optical morphology of this sample of spatially resolved galaxies, both parametrically, identifying on average their stellar light distributions follow an exponential disc with a median Sérsic index of  $\langle n \rangle = 1.37 \pm 0.12$  (Section 3.2.1), and non-parametrically, showing that the galaxies in the KGES sample have symmetrical and clumpy morphologies (Section 3.2.3).

Exploiting the KMOS observations, we showed the kinematics of the KGES galaxies align with that of star-forming discs with well-defined ordered rotation (Fig. 4) with a median rotational velocity of  $\langle V_{2R_h} \rangle = 102 \pm 8 \text{ km s}^{-1}$ . A full catalogue of all observable properties measured from the KGES galaxies will be published in Tiley et al. (in preparation). In the following sections we use these observed properties of the KGES galaxies to analyse more derived quantities (e.g. specific angular momentum) and explore the connection between a galaxy's gas dynamics and rest-frame optical morphology.

## 4 DISCUSSION

### 4.1 The specific angular momentum of gas discs at $z \sim 1.5$

The correlation between specific stellar angular momentum and stellar mass is well established at  $z \sim 0$  (e.g. Fall & Efstathiou 1980; Posti et al. 2018) with higher stellar mass galaxies having higher specific angular momentum according to a scaling  $j_* \propto M_*^{2/3}$  (e.g. Fall 1983; Mo et al. 1998). Romanowsky & Fall (2012) updated the work by Fall (1983) with new observations of galaxies spanning a range of morphologies, confirming that for a fixed stellar mass, galaxy discs have a factor 5–6 $\times$  more angular momentum than spheroidal galaxies.

In Fig. 8, we plot the specific stellar angular momentum of the KGES sample as a function of their stellar mass. The median specific stellar angular momentum in the sample is  $\langle j_* \rangle = 391 \pm 53 \text{ km s}^{-1} \text{ kpc}$  with a 16–84th percentile range of  $j_* = 74-1085 \text{ km s}^{-1} \text{ kpc}$ . To place the KGES sample in context with the  $j_*-M_*$  plane, we compare the specific stellar angular momentum to other surveys of star-forming galaxies across a range of redshift. We include the Fall & Romanowsky (2013) pure disc sample of star-forming  $z \sim 0$  galaxies as well the KROSS (Harrison

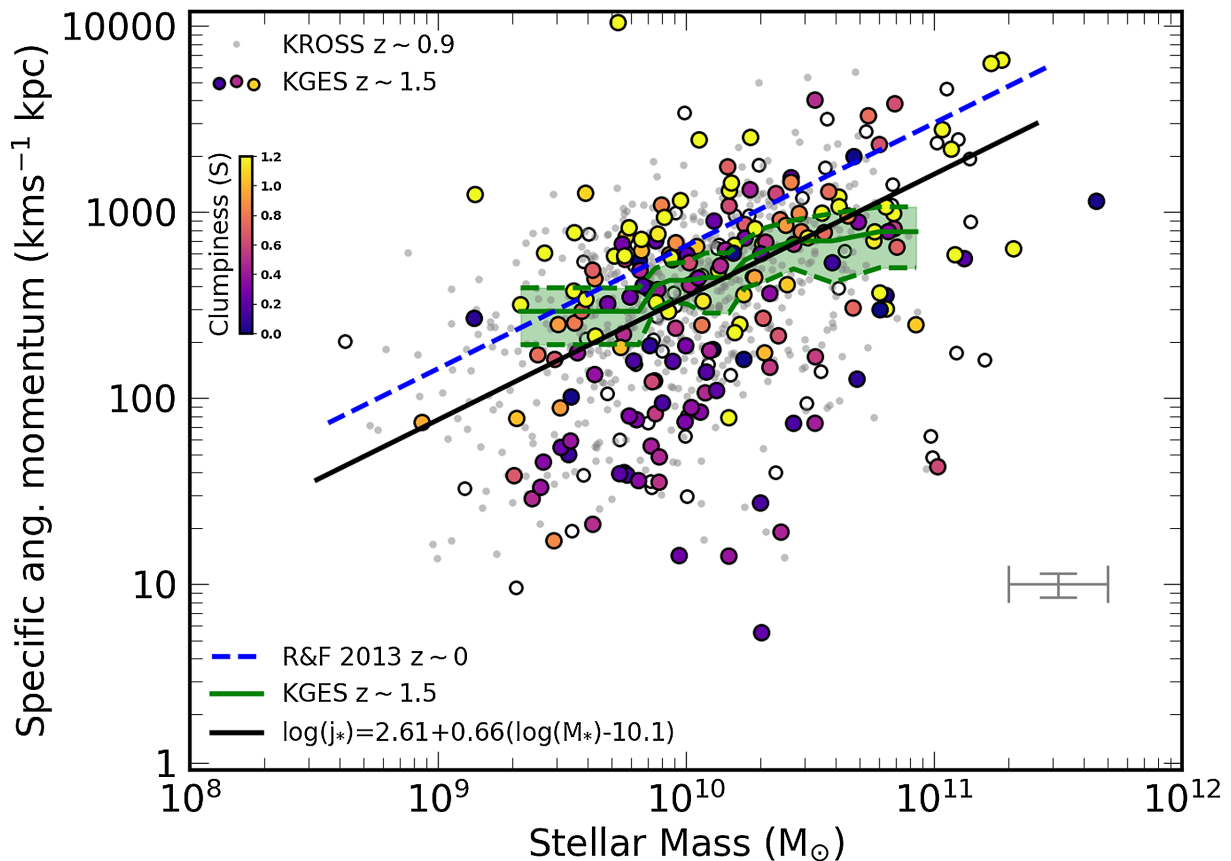


**Figure 8.** Specific stellar angular momentum as a function of stellar mass. Clumpiness parameter of the KGES sample shown by the colour map. Lower H  $\alpha$  S/N (Quality 3) objects are shown by the open circles. KROSS  $z \sim 0.9$  sample shown as grey points in the background (Harrison et al. 2017). A parametric fit to the disc component of  $z \sim 0$  galaxies as derived by Fall & Romanowsky (2013) is shown by the blue line. The green shaded region and the dashed lines indicate the median trend of the KGES galaxies and their  $1\sigma$  scatter. The black line is a fit to the KGES data of the form  $\log_{10}(j_*) = \alpha + \beta(\log_{10}(M_*/M_\odot) - 10.10)$ , with the slope fixed to  $\beta = 0.66$  and a derived intercept of  $\alpha = 2.61$ . The KGES sample occupy a similar region of parameter space to KROSS but offset to lower angular momentum for given stellar mass than Fall & Romanowsky (2013)  $z \sim 0$  pure disc galaxies. The galaxies show a trend of increasing specific angular momentum with stellar mass while having a broad range of specific stellar angular momentum at fixed stellar mass that correlates with the clumpiness of the galaxy.

et al. 2017)  $z \sim 0.9$  sample. On average, for a given stellar mass, KGES galaxies occupy a similar region of parameter space to the KROSS sample while being offset to lower specific stellar angular momentum than the Fall & Romanowsky (2013)  $z \sim 0$  sample. It should be noted that other studies have also suggested minimal evolution in the zero-point offset in the  $j_* - M_*$  from  $z \sim 1$  to  $z \sim 0$  (e.g. Marasco et al. 2019).

To quantify the specific stellar angular momentum and stellar mass plane in the KGES sample, we fit a relation of the form  $\log_{10}(j_*) = \alpha + \beta(\log_{10}(M_*/M_\odot) - 10.10)$ . At low redshift the relationship between galaxy and halo angular momentum is approximated by  $j_*/j_{\text{halo}} \propto (M_*/M_{\text{halo}})^{2/3}$  (e.g. Romanowsky & Fall 2012; Obreschkow et al. 2015; Fall & Romanowsky 2018; Sweet et al. 2019; Posti et al. 2019). A power-law index of  $\beta = 0.66$  at high-redshift implies that dark matter haloes in a  $\Lambda$ CDM Universe are scale free. However, the stellar mass fraction ( $M_*/M_{\text{halo}}$ ) varies strongly with halo mass (e.g. Behroozi et al. 2019; Sharma & Theuns 2019) and therefore it is not clear that the exponent should also hold for stars. To test whether this scaling holds in high-redshift galaxies, we fit the  $j_* - M_*$  plane using a chi-squared minimization to find the best-fitting parameters of the linear model. For the KGES galaxies, with an unconstrained fit, we derive a slope of  $\beta = 0.53 \pm 0.10$  with a normalization of  $\alpha = 2.63 \pm 0.04$ .

The slope of the  $j_* - M_*$  plane is consistent within  $1.3\sigma$  of that derived from the assumption  $j_*/j_{\text{halo}} \propto (M_*/M_{\text{halo}})^{2/3}$ . Given this similarity for the following analysis we make the assumption and fix  $\beta = 0.66$  (i.e. assuming  $j_*/j_{\text{halo}} \propto (M_*/M_{\text{halo}})^{2/3}$ ), which allows comparison to lower redshift surveys (e.g. Fall & Romanowsky (2013)). We refit the  $j_* - M_*$  plane, constraining the slope to be  $\beta = 0.66$  and derive a normalization  $\alpha = 2.60 \pm 0.03$  for all 235 spatially resolved KGES galaxies. We note that the parametrization of the  $j_* - M_*$  plane is dependent on the uncertainties on the stellar mass which can be significant (e.g. Pforr, Maraston & Tonini 2012). We have adopted a conservative  $\pm 0.2$  dex uncertainty as demonstrated by Mobasher et al. (2015) to account for systematic effects.

Across the whole sample of targeted 288 KGES galaxies, there is a range of H  $\alpha$  signal to noise, with some galaxies having very low signal to noise kinematics and rotation curves. Subsequently, dynamical measurements of these galaxies are more uncertain. To understand the effect these lower quality targets have on our analysis, we define four quality flags with the following kinematic criteria that is based on the signal to noise of the galaxy-integrated H  $\alpha$  emission and the extrapolation of the observed rotation curve.

- (i) Quality 1: H  $\alpha > 50$  S/N and  $R_{\text{last}}/2R_h > 1$

- (ii) Quality 2:  $20 < H\alpha \text{ S/N} < 50$  and  $R_{\text{last}}/2R_h > 1$
- (iii) Quality 3:  $H\alpha \text{ S/N} < 20$  or  $0.3 < R_{\text{last}}/2R_h < 1.5$
- (iv) Quality 4:  $H\alpha \text{ S/N} < 1$  or  $R_{\text{last}}/2R_h < 0.1$

Of the 288 galaxies, 201 are classified as either quality 1 (107 galaxies) or quality 2 (94 galaxies). 42 galaxies are labelled as quality 3 while 45 galaxies have the lowest quality kinematic and broad-band data and are labelled quality 4. If we fit  $\log_{10}(j_*) = \alpha + \beta (\log_{10}(M_*/M_\odot) - 10.10)$  to just quality 1 and 2 galaxies we establish a normalization of  $\alpha = 2.61$ , indicating that including only high quality targets gives the same normalization as the full sample.

## 4.2 Dynamics and angular momentum

With a sample of 235 galaxies with spatially resolved gas kinematics we can investigate the scatter about the median  $j_* - M_*$  trend that is driven by physical processes in a galaxy's evolution. In this section, we explore how the scatter correlates with the galaxy's dynamical properties (e.g. rotation velocity, turbulence, star formation rate surface density).

To quantify the position of a galaxy in the  $j_* - M_*$  plane we define the parameter,  $\Delta j$  as  $\Delta j = \log_{10}(j_{\text{gal}}) - \log_{10}(j_{\text{fit}})$ . Where  $j_{\text{gal}}$  is the specific stellar angular momentum of the galaxy and  $j_{\text{fit}}$  is the specific stellar angular momentum of the parametric fit to the survey at the same stellar mass (see Romanowsky & Fall (2012) Equation 12). Galaxies that lie above the parametric fit of the form  $\log_{10}(j_*) = 2.61 + 0.66 (\log_{10}(M_*/M_\odot) - 10.10)$  will have positive  $\Delta j$  while those galaxies that lie below the line will have negative  $\Delta j$  values.

In Fig. 9, we show the correlation between velocity dispersion ( $\sigma_0$ ) and  $\Delta j$ , with the galaxies coloured by their  $H\alpha$  specific star formation rate. The KROSS  $z \sim 0.9$  sample is shown for comparison. We identify no correlation between velocity dispersion and  $\Delta j$ , with a Spearman rank coefficient of  $r = -0.09$ . This indicates that galaxies of higher angular momentum do not necessarily have less turbulence and thinner discs. This appears to be the case at both  $z \sim 0.9$  and  $z \sim 1.5$ . We have also identified no significant correlation between the  $H\alpha$  specific star formation rate and  $\Delta j$  of KGES galaxies indicating that more turbulent galaxies with higher specific star formation rates do not necessarily have lower specific angular momentum.

In Fig. 9, we also show the star formation rate surface density ( $\Sigma_{\text{SFR}}$ ) as a function of the ratio of rotation velocity to velocity dispersion ( $V(2R_h)/\sigma_0$ ) for both KGES and KROSS samples, identifying a Spearman rank coefficient of  $r = -0.42$ . Galaxies that are dispersion dominated (low  $V(2R_h)/\sigma_0$ ), tend to have higher  $\Sigma_{\text{SFR}}$ , and low specific angular momentum (negative  $\Delta j$ ).

## 4.3 Morphology and angular momentum

Now that we have explored the connection between a galaxy's dynamics and its specific angular momentum, identifying galaxies that are more rotation dominated generally have higher angular momentum and lower star formation rate surface densities, we now explore the connection to the galaxy's parametrized rest-frame optical morphology.

In the local Universe strong correlations have been identified at fixed stellar mass between a galaxy's Sérsic index, stellar bulge to total ratio and specific angular momentum. Both Romanowsky & Fall (2012) and Cortese et al. (2016) identified that the more bulge dominated, spheroidal, a system is, the lower its specific angular

momentum for a given stellar mass will be. The scatter about the  $j_* - M_*$  plane at low redshift is driven by the variation in Sérsic index and stellar bulge to total ratio of the galaxies (e.g. Obreschkow & Glazebrook 2014; Fall & Romanowsky 2018; Sweet et al. 2018).

As as first approach, we adopt the visual classifications of galaxy morphology from Huertas-Company et al. (2015), who use convolutional neural networks to categorize the *HST* F160W morphology of 50 000 galaxies in the CANDELS survey. By training the algorithm on the GOOD-S CANDELS field, which has been previously visually classified by Kartaltepe et al. (2016), Huertas-Company et al. (2015) were able to accurately classify a galaxies' morphology with a 1 per cent mis-classification. We cross-match the KGES survey in the overlapping region with galaxies in the Huertas-Company et al. (2015) sample, identifying 122 galaxies. Of which, 84 galaxies have a visual classification as either spheroidal, disc, or peculiar morphology. The remaining 34 galaxies were not definitively classified by the neural network.

In Fig. 9, we show the relation between star formation rate surface density ( $\Sigma_{\text{SFR}}$ ) and the ratio of rotation velocity to velocity dispersion ( $V(2R_h)/\sigma_0$ ), with KGES galaxies coloured by their visual morphologies. More dispersion-dominated galaxies with higher  $\Sigma_{\text{SFR}}$  tend to be the more spheroidal with  $\langle V(2R_h)/\sigma_0 \text{ spheroidal} \rangle = 1.19 \pm 0.68$ . Rotation-dominated KGES galaxies (high  $V(2R_h)/\sigma_0$ ), tend to have lower  $\Sigma_{\text{SFR}}$  with high specific angular momentum, and have visual morphologies that appear as either discs or peculiar systems with  $\langle V(2R_h)/\sigma_0 \text{ disc} \rangle = 2.33 \pm 0.40$ , while  $\langle V(2R_h)/\sigma_0 \text{ peculiar} \rangle = 2.22 \pm 0.37$ .

To understand this link between morphology and angular momentum further, we show the specific stellar angular momentum stellar mass plane for the KGES survey, in Fig. 10, with galaxies coloured by their 'visual morphology'. Galaxies classified as spheroidal appear to lie clearly below the fit, as expected due to their smaller stellar continuum sizes, while galaxies labelled as discs appear to lie above the fit. Galaxies labelled as peculiar appear to be scattered about the best-fitting line highlighting the diversity of the peculiar galaxies morphology and kinematic state.

For galaxies scattered about the median trend, in the specific stellar angular momentum stellar mass plane, in Fig. 10, we show the *HST* wide field camera colour images. For a given stellar mass, those galaxies that have the highest angular momentum have more prominent discs with the presence of spiral arms. While galaxies with the lowest angular momentum are much more spheroidal, as expected. We note however that the spheroidal galaxies may appear to have low angular momentum because their rotation is unresolved in the KMOS observations. The higher stellar mass, high angular momentum KGES galaxies show strong signs of significant bulge components in their colour images. This is in agreement with the evolution of stellar mass and stellar bulge-to-total ratio identified in both simulations (e.g. Trayford et al. 2018) and observations (e.g. Gillman et al. 2019).

### 4.3.1 Quantized morphology and dynamics

To interpret this connection between morphology and angular momentum further, we explore the correlation between a galaxy's position in the  $j_* - M_*$  plane and its quantized (both parametric and non-parametric) morphology as derived in Section 3.2.1. In Fig. 11, we plot  $\Delta j$  as a function of Sérsic index, stellar bulge to total ratio ( $\beta_*$ ), clumpiness, asymmetry, and concentration for KGES galaxies with CANDELS F814W *HST* imaging. We select this subsample



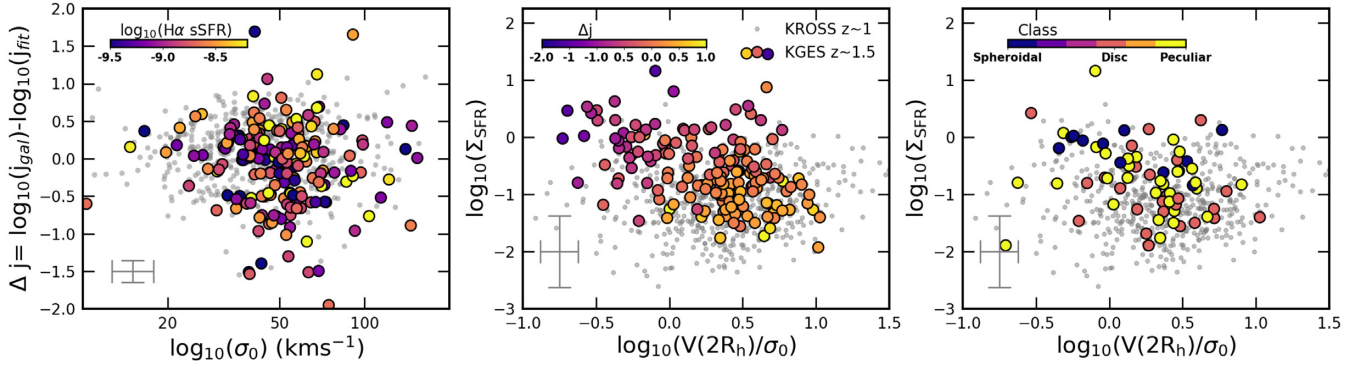


**Figure 9.** Left-hand panel: The angular momentum offset from the parametric fit  $\log_{10}(j_*) = 2.61 + 0.66(\log_{10}(M_*/M_\odot) - 10.10)$  ( $\Delta j$ ) as a function of velocity dispersion ( $\sigma_0$ ) coloured by the  $\text{H}\alpha$  specific star formation rate. We identify no correlation between a galaxies position in the  $j_* - M_*$  plane and the velocity dispersion or  $\text{H}\alpha$  specific star formation rate (e.g. turbulence of the interstellar medium) of the galaxy. Middle and Right-hand panel: The  $\text{H}\alpha$  star formation rate surface density ( $\Sigma_{\text{SFR}}$ ) as a function of the ratio of rotation velocity to velocity dispersion ( $V(2R_h)/\sigma_0$ ). The middle panel is coloured by  $\Delta j$ , while the right-hand panel is coloured by visual morphological class, as defined in Section 4.3. In all three panels the KROSS  $z \sim 0.9$  sample is shown by the grey points. The median uncertainty is shown in the lower left corner of each panel. Galaxies of higher  $\Sigma_{\text{SFR}}$  are more dispersion dominated, with lower specific stellar angular momentum, resembling more spheroidal morphologies. Disc galaxies have lower  $\Sigma_{\text{SFR}}$ , are more rotation dominated, and have higher specific stellar angular momentum while peculiar galaxies tend to have high  $\Sigma_{\text{SFR}}$  while being rotation dominated, with high specific stellar angular momentum.

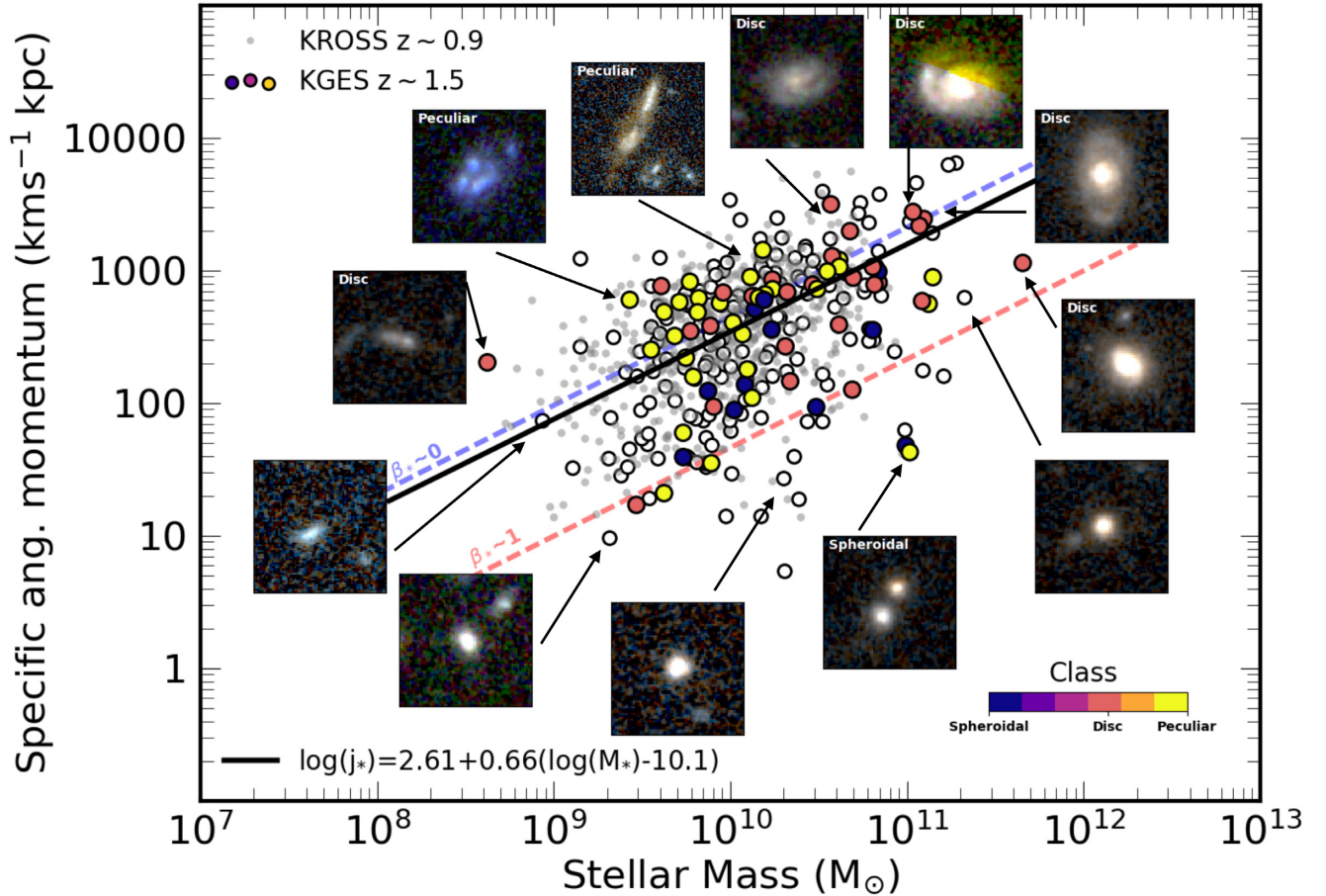


**Figure 10.** Specific stellar angular momentum as a function of stellar mass. Visual morphology of the KGES sample shown by the colour map. Quality 3 and 4 objects shown by open circles. KROSS  $z \sim 0.9$  sample shown as grey points in the background Harrison et al. (2017). The black line is a fit to the KGES data of the form  $\log_{10}(j_*) = \alpha + \beta(\log_{10}(M_*/M_\odot) - 10.10)$ , with the slope fixed to  $\beta = 0.66$  and a derived intercept of  $\alpha = 2.61$ . Fixed stellar bulge to total ratio ( $\beta_*$ ) lines from Romanowsky & Fall (2012) are shown by the blue and red lines. *HST* wide field camera colour images of some of the galaxies are shown around the edge of the figure with the visual class of the galaxy indicated. There is a clear correlation between the position of the galaxy in the specific stellar angular momentum stellar mass plane and the galaxies visual morphology.



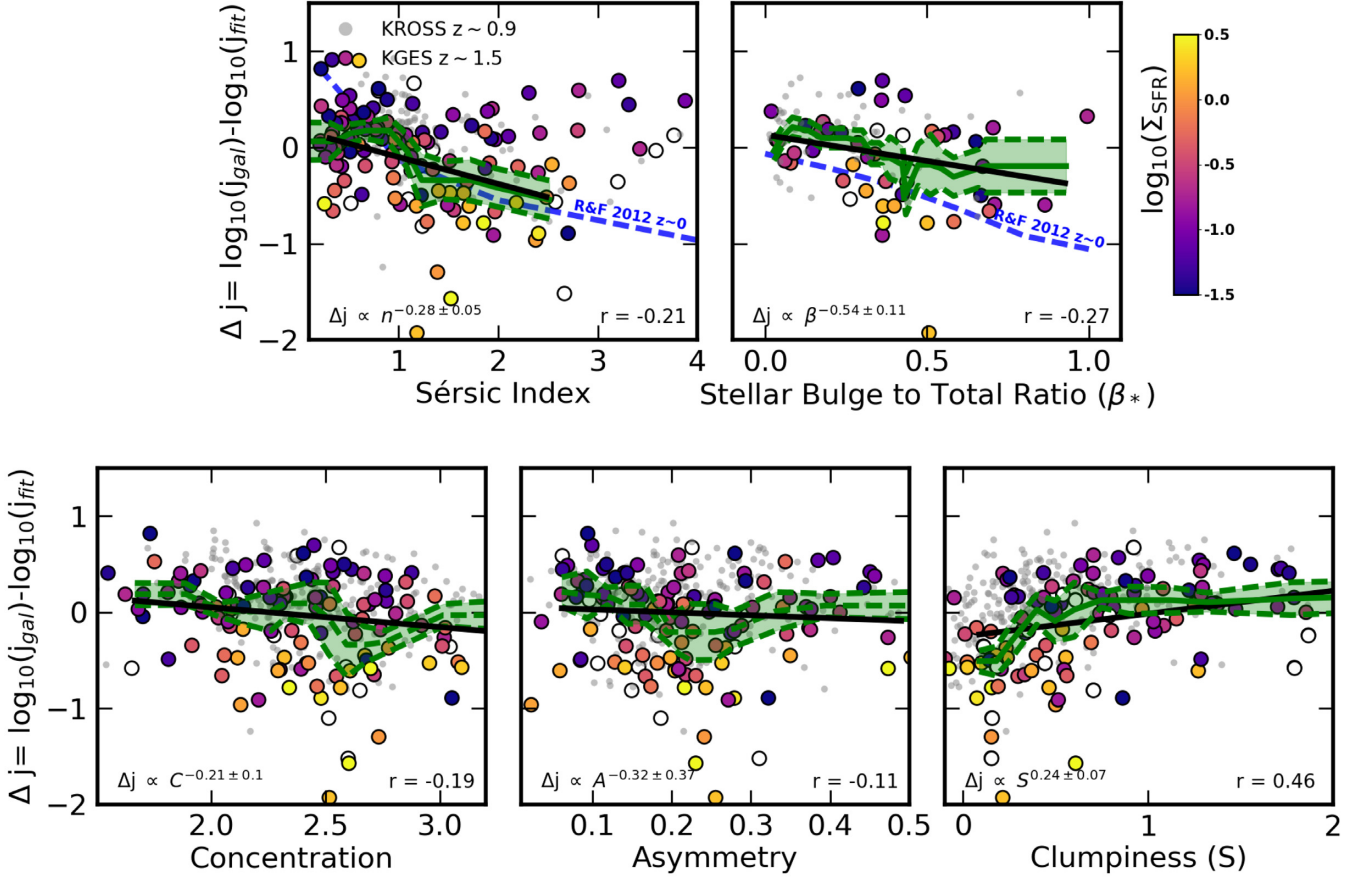


**Figure 11.** The angular momentum offset from the parametric fit  $\log_{10}(j_*) = 2.61 + 0.66(\log_{10}(M_*/M_\odot) - 10.10)$  ( $\Delta j$ ) as a function of Sérsic index, stellar bulge to total ratio ( $\beta_*$ ), clumpiness, asymmetry, and concentration for the KGES galaxies measured in the CANDELS F814W *HST* band. The open circles show quality 3 and 4 galaxies, while quality 1 and 2 galaxies are coloured by their  $H\alpha$  star formation rate surface density ( $\Sigma_{\text{SFR}}$ ). In the top two panels we show a  $z \sim 0$  comparison sample from Romanowsky & Fall (2012). The KROSS survey is shown by the grey points in the background, with  $\Delta j$  measured relative to the parametric fit to the KROSS galaxies. The green line and shaded region indicates a running median and  $1\sigma$  error to the KGES quality 1 and 2 galaxies, and the black line is a parametric fit. Galaxies in the KGES sample with high specific angular momentum for a given stellar mass, on average have lower Sérsic index and stellar bulge to total ratio while being more clumpy and asymmetrical.

of KGES galaxies with the highest quality data, to allow accurate comparison between the integrated parametric and non-parametric measures of morphology.

The Sérsic index of KGES galaxies has a weak negative correlation with a galaxy’s position in the  $j_* - M_*$  plane of the form  $\Delta j \propto n^{-0.27 \pm 0.05}$  with a Spearman rank coefficient of  $r = -0.21$ , and this weakens slightly with the inclusion of galaxies from KROSS. Galaxies of higher Sérsic index at  $z \sim 1.5$  have lower  $\Delta j$  and this appears to be less common at  $z \sim 0.9$ . We show the relation between  $\Delta j$  and Sérsic index for  $z \sim 0$  galaxies from Romanowsky & Fall (2012). The parametrization of the relation is taken from Cortese et al. (2016) who established the  $j_* - M_*$ - $n$  relation for the SAMI survey. We note the parametrization derived in Cortese et al. (2016) is for a morphologically diverse population of both quiescent and star-forming low-redshift galaxies, and therefore should not be compared directly to our sample of star-forming selected high-redshift galaxies. The relation between stellar mass, Sérsic index, and specific angular momentum can be parametrized as

$$\log(j/\text{kpc km s}^{-1}) = a \times \log(M_*/M_\odot) + b \times \log(n) + c, \quad (14)$$

where  $a = 1.05$ ,  $b = -1.38$ , and  $c = -8.18$ . Using the sample of  $z \sim 0$  galaxies presented in Romanowsky & Fall (2012), we establish

the relation between  $\Delta j$  and Sérsic index for  $z \sim 0$  galaxies indicated by the dashed line in Fig. 11. The relation is very similar to that identified in the KGES sample at  $z \sim 1.5$ , with higher Sérsic index galaxies having lower specific angular momentum.

The stellar bulge to total ratios ( $\beta_*$ ) for both KROSS and KGES galaxies are taken from Dimauro et al. (2018) who derive  $\beta_*$  using a multiwavelength machine learning algorithm for  $\sim 18\,000$  galaxies in the *HST* CANDELS field selected to have an *F160W* magnitude of  $< 23$  in the redshift range  $z = 0-2$ . In Fig. 11, we plot  $\Delta j$  as a function of  $\beta_*$ , derived from only *F160W HST* imaging, and identify a moderate negative correlation of  $\Delta j \propto \beta_*^{-0.27 \pm 0.36}$  and a Spearman rank coefficient of  $r = -0.27$ , with lower angular momentum galaxies having higher bulge to total ratios. A similar correlation is present in KROSS at  $z \sim 0.9$ , and when the two surveys are combined we derive  $\Delta j \propto \beta_*^{-0.51 \pm 0.18}$ . This is in agreement with the correlation between  $\Delta j$  and  $n$ , with higher Sérsic index stellar light distributions corresponding to more bulge-dominated systems.

Fall & Romanowsky (2018) identify a strong correlation between a galaxy’s position in the specific stellar angular momentum stellar mass plane and stellar bulge to total ratio in a sample of local galaxies. Galaxies with fixed bulge to total ratio follow parallel tracks in the  $j_* - M_*$  plane, with  $\beta_* \sim 0$  (Sc, Sb) galaxies having the highest normalization and  $\beta_* \sim 1$  (E) galaxies having the lowest

(Fig. 10). They conclude that the  $j_*-M_*$ - $\beta_*$  scaling provides an alternative to the Hubble classification of galaxy morphology. In Fig. 11, we plot the correlation between  $\Delta j$  and bulge to total ratio derived from the relations and galaxies presented in Romanowsky & Fall (2012). The  $z \sim 0$  relation is offset to lower angular momentum than our  $z \sim 1.5$  sample, with more bulge-dominated galaxies having lower angular momentum, than a galaxy with the same  $\beta_*$  at  $z \sim 1.5$ . We note the scatter in the  $\Delta j$ - $\beta_*$  and  $\Delta j$ - $n$  plane maybe driven by a combination of resolution effects, whereby we do not resolve the rotation in spheroidal objects, nor do we resolve the kinematics on sub-kpc scales revealing potential merging kinematic components. Equally, the galaxy population may contain a number of massive early-type galaxies with evolved bulges that have high Sérsic index and bulge to total ratios as well as the dominant population of spheroidal star-forming galaxies that have a high central star formation rates.

The position of a galaxy in the  $j_*-M_*$  shows a weak negative correlation with the concentration of the galaxy's stellar light with  $\Delta j \propto C^{-0.2 \pm 0.1}$  ( $r = -0.19$ ). This is as expected as more concentrated galaxies have higher Sérsic indices and higher bulge to total ratios. The asymmetry of the galaxy however shows no significant correlation, with  $\Delta j \propto A^{-0.32 \pm 0.37}$  and a Spearman rank coefficient of  $r = -0.11$ . The clumpiness of the light distribution however indicates a moderate positive trend ( $\Delta j \propto S^{0.24 \pm 0.07}$ ) with  $\Delta j$  with a Spearman rank coefficient of  $r = -0.46$ . This indicates galaxies that are more clumpy and less concentrated have higher angular momentum than the average galaxy in the survey for a given stellar mass, regardless of the asymmetry of the light profile. The correlation with the symmetry of the galaxy is less well constrained due to the large uncertainty on the exponent. As shown in Fig. 11, galaxies with higher star formation rate surface density have lower specific angular momentum at fixed stellar mass.

We infer that the correlations in Figs 9 and 11 could be driven by spheroidal objects with low angular momentum being very concentrated and smooth, while high angular momentum disc galaxies with spiral arms and significant bulge components are more clumpy and but have similar levels of asymmetry. Peculiar galaxies in the KGES sample also are very clumpy and asymmetrical but still maintain high specific angular angular momentum.

#### 4.3.2 Qualitative morphology and dynamics

As shown in Fig. 11, high specific angular momentum galaxies tend to have higher clumpiness and are less bulge dominated with lower Sérsic indices. Fig. 10 shows that high angular momentum galaxies generally have disc dominated or peculiar morphologies. Using the visual classifications established from Huertas-Company et al. (2015), the medium clumpiness of peculiar galaxies in the KGES sample is  $\langle S_{\text{peculiar}} \rangle = 0.70 \pm 0.27$  while for disc galaxies  $\langle S_{\text{disc}} \rangle = 0.58 \pm 0.10$ . The Sérsic index of peculiar systems is  $\langle n_{\text{peculiar}} \rangle = 0.88 \pm 0.14$  while disc galaxies have a medium value of  $\langle n_{\text{disc}} \rangle = 1.19 \pm 0.28$ . The quantitative, parametric and non-parametric, measures of a galaxies morphology are successful in isolating spheroidal systems however they are less reliable in distinguishing peculiar galaxies from disc-dominated ones. Consequently, we next focus on the dynamical differences between the visual morphological classes in the KGES survey.

Before we compare the kinematic properties of galaxies with different morphologies, we first infer an approximation for the stability of the gas disc in each galaxy. To analyse the interplay between the rotational velocity, velocity dispersion, and star formation rate

surface density, we quantify the average stability of the galactic disc in each galaxy against local gravitational collapse, as parametrized by the Toomre stability parameter.

From the Jeans criterion, a uniform density gas cloud will collapse if its self-gravity can overcome the internal gas pressure (Jeans 1902). However, in a galactic disc the differential rotation of the galaxy provides additional support to the internal gas pressure of the gas cloud. If the gas cloud becomes too large it will be torn apart by shear, faster than the gravitational free fall time (Toomre 1964). For a thin gas disc, this stability criterion of the balance between shear, pressure support, and self-gravity can be quantified by the Toomre  $Q_{\text{gas}}$  parameter which is defined as

$$Q_{\text{gas}} = \frac{\sigma_{\text{gas}} \kappa}{\pi G \Sigma_{\text{gas}}}, \quad (15)$$

where  $\sigma_{\text{gas}}$  is the line-of-sight velocity dispersion,  $\Sigma_{\text{gas}}$  is the gas surface density of the disc, and  $\kappa$  is the epicyclic frequency of the galaxy and is approximated as  $\kappa = aV/R$ , within which  $V$  is the rotational velocity of the disc at radius  $R$  and  $a = \sqrt{2}$  for a flat rotation curve. The rotational velocity and velocity dispersion are measured at  $2R_h$  from the kinematic profiles of each galaxy (Section 3.3).

We use the Kennicutt–Schmidt (KS) relation (Kennicutt 1998) to infer the gas surface density ( $\Sigma_{\text{gas}}$ ). The KS relation is defined as

$$\left( \frac{\Sigma_{\text{SFR}}}{\text{M}_{\odot} \text{ yr}^{-1} \text{ kpc}^{-2}} \right) = A \left( \frac{\Sigma_{\text{gas}}}{\text{M}_{\odot} \text{ pc}^{-2}} \right)^n, \quad (16)$$

where  $A = 1.5 \times 10^{-4} \text{ M}_{\odot} \text{ yr}^{-1} \text{ pc}^{-2}$  and  $n = 1.4$ . Galaxies with  $Q_{\text{gas}} < 1$  are unstable to local gravitational collapse and will fragment into clumps. Galaxies with  $Q_{\text{gas}} > 1$  have sufficient rotational support for the gas and are stable against collapse. We are assuming that the galaxy averaged  $Q_{\text{gas}}$  is a good approximation of the average disc stability as we do not spatially resolve  $Q_{\text{gas}}$ . We note however that we are primarily using  $Q_{\text{gas}}$  to differentiate across the KGES sample, and it is the relative value of  $Q_{\text{gas}}$  that is important rather than focusing on the specific stability of each galaxy. We also note that this parameter only describes the stability of a pure gas disc. The stability of a disc composed of gas and stars is given by the total Toomre  $Q_t \approx 1/(1/Q_{\text{gas}} + 1/Q_{\text{stars}})$  and describes stability against Jeans clumps. For a more in-depth analysis of the relation between Toomre  $Q$  and galaxy properties see Romeo & Mogotsi (2018).

We measure the Toomre  $Q_{\text{gas}}$  parameter in all 243 KGES galaxies identifying a median stability parameter of  $\langle Q_{\text{gas}} \rangle = 0.63 \pm 0.10$ . We note this is not the true value of disc stability for the KGES sample since we do not take into account the disc thickness nor the stability of the stellar component (e.g. Wang & Silk 1994; Romeo & Wiegert 2011).

To understand the dynamical differences between galaxies of different morphologies, we separate out the spheroidal, disc, and peculiar galaxies and study their dynamical and morphological properties. In Fig. 12, we show example *HST* colour images of spheroidal, disc, and peculiar galaxies in the KGES sample, as well as the distributions of various morphological and kinematic parameters. In comparison to the disc galaxies in the KGES sample, spheroidal galaxies on average have lower specific angular momentum and are more dispersion dominated but have velocity dispersions that are comparable:  $\langle \sigma_{0, \text{spheroidal}} \rangle = 56 \pm 9 \text{ km s}^{-1}$  and  $\langle \sigma_{0, \text{disc}} \rangle = 58 \pm 6 \text{ km s}^{-1}$ . The spheroidal galaxies are more unstable to local gravitational collapse with higher  $H\alpha$  star formation rate surface densities, where  $\langle \Sigma_{\text{SFR, disc}} \rangle = 0.09 \pm 0.04 \text{ M}_{\odot} \text{ yr}^{-1} \text{ kpc}^{-2}$  compared to  $\langle \Sigma_{\text{SFR, spheroidal}} \rangle = 0.77 \pm 0.21 \text{ M}_{\odot} \text{ yr}^{-1} \text{ kpc}^{-2}$ . Morphologically, they are less clumpy and more concentrated, but

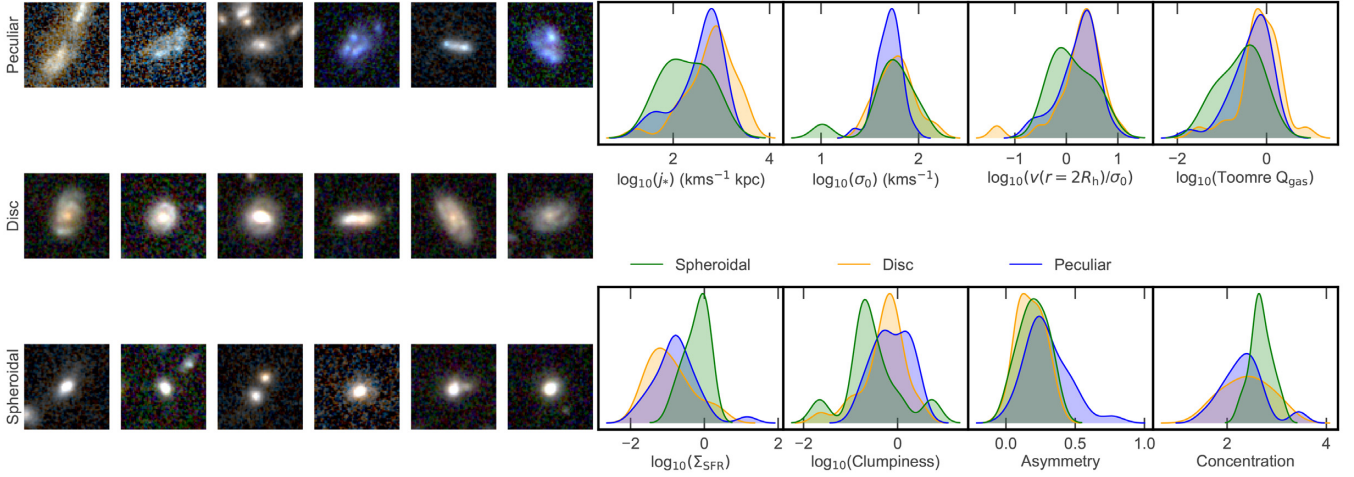


**Figure 12.** *HST* colour images of KGES galaxies. Spheroidal, disc, and peculiar morphological classes (left) with the kernel density distribution of specific angular momentum ( $j_*$ ), velocity dispersion ( $\sigma_0$ ), ratio of rotation velocity to velocity dispersion ( $V(2R_h)/\sigma_0$ ), disc stability ( $Q_{\text{gas}}$ ),  $\text{H}\alpha$  star formation rate surface density ( $\Sigma_{\text{SFR}}$ ), clumpiness, asymmetry, and concentration (right). The velocity dispersion and concentration of spheroidal, disc, and peculiar galaxies are very similar. Spheroidal galaxies have lower specific stellar angular momentum, are more dispersion dominated, have lower Toomre  $Q_{\text{gas}}$ , are less clumpy, more asymmetrical but have higher  $\Sigma_{\text{SFR}}$  than disc-like galaxies. Peculiar galaxies on average have the same specific stellar angular momentum, are similarly rotation dominated, but have lower Toomre  $Q_{\text{gas}}$  and are more clumpy, more asymmetrical but with higher  $\Sigma_{\text{SFR}}$  than disc-like galaxies.

have very similar asymmetries with  $\langle A_{\text{spheroidal}} \rangle = 0.19 \pm 0.04$  and  $\langle A_{\text{disc}} \rangle = 0.19 \pm 0.03$ .

Taking the properties of morphologically peculiar galaxies in the KGES sample in comparison to morphologically disc-dominated galaxies, we establish that on average they have comparable levels of specific angular momentum, velocity dispersion, and are equally rotation dominated with  $\langle V(2R_h)/\sigma_0 \rangle_{\text{disc}} = 2.33 \pm 0.40$  and  $\langle V(2R_h)/\sigma_0 \rangle_{\text{peculiar}} = 2.22 \pm 0.37$ . A peculiar galaxy has comparable stability gravitational collapse to a disc galaxy, with higher  $\Sigma_{\text{SFR}}$  where  $\langle \Sigma_{\text{SFR, peculiar}} \rangle = 0.16 \pm 0.04 \text{ M}_{\odot} \text{ yr}^{-1} \text{ kpc}^{-2}$ . Morphologically peculiar galaxies are more clumpy and asymmetrical with slightly higher levels of concentration with  $\langle C_{\text{peculiar}} \rangle = 2.33 \pm 0.09$  while  $\langle C_{\text{disc}} \rangle = 2.38 \pm 0.12$ .

#### 4.3.3 Interpretation – the high-redshift galaxy demographic

From Fig. 12, for a given stellar mass, a galaxy with low specific angular momentum is likely to be spheroidal, while a galaxy with high specific angular momentum and high star formation rate surface density is likely to be peculiar. High specific angular momentum galaxies with low star formation rate surface density, on average, tend to have disc-like morphologies.

Assuming the galaxies in the KGES sample follow the KS relation (e.g. Gnedin & Kravtsov 2010; Freundlich et al. 2013; Orr et al. 2018; Sharda et al. 2018), galaxies with higher star formation rate surface densities imply higher gas surface densities and hence likely high gas fractions. Recent hydrodynamical zoom-in simulations with the FIRE project (Hopkins et al. 2014, 2018) have shown that the stellar morphology and kinematics of Milky Way mass galaxies correlate more strongly with the gaseous histories of the galaxies (Garrison-Kimmel et al. 2018), in particular around the epoch the galaxy has formed half of its stars (e.g.  $z \sim 1.5$  Gillman et al. 2019). This indicates the gas content of high-redshift galaxies plays a crucial in their evolution. The balance between the self-gravity of the gas clouds and the shear due to the galaxy’s differential rotation determines the local gravitational stability of the disc.

Fig. 12 indicates that peculiar galaxies on average are as stable as disc systems with  $\langle Q_{\text{g, disc}} \rangle = 0.70 \pm 0.20$  while  $\langle Q_{\text{g, peculiar}} \rangle = 0.64 \pm 0.13$ , but have similar velocity dispersions. Peculiar systems have higher star formation rate surface density, thus given that Toomre  $Q_{\text{g}} \propto \kappa/\Sigma_{\text{SFR}}$ , we would expect a ‘stable’ peculiar galaxy to have a higher  $\kappa$  value.

We measure the outer gradient of each galaxy’s  $\text{H}\alpha$  rotation curve in the KGES sample, between  $r = R_h$  and  $r = 2R_h$  as a proxy for the  $\kappa$  value, given that Toomre  $Q_{\text{g}}$  is normally measured radially. In this radial range the impact of beam smearing on the rotation curve is reduced compared to the central regions. It has been shown that the shape of a galaxy’s rotation curve is strongly correlated with the morphology of a galaxy at  $z = 0$  (e.g. Sofue & Rubin 2001), with galaxies of different Hubble-type morphologies from Sa to Sd having characteristically different rotation curves, that reflect the gravitational potential of the galaxy.

Peculiar galaxies have a median gradient of  $\langle \frac{\delta v_{\text{H}\alpha}}{\delta r} |_{r=R_h-2R_h} \rangle = 3 \pm 2 \text{ km s}^{-1} \text{ kpc}^{-1}$  while disc galaxies have  $\langle \frac{\delta v_{\text{H}\alpha}}{\delta r} |_{r=R_h-2R_h} \rangle = 4 \pm 2 \text{ km s}^{-1} \text{ kpc}^{-1}$ . The outer gradients of the peculiar galaxies in the KGES sample, at a fixed mass, are very similar to that of disc galaxies, which is reflected in their lower Toomre  $Q_{\text{g}}$ . This suggests at a fixed stellar mass, high-redshift peculiar galaxies are dynamically differentiated from disc-dominated galaxies, by their higher  $\Sigma_{\text{SFR}}$  and higher gas fractions. The peculiar galaxies on average have similar specific angular momentum to disc galaxies, so to evolve to a well-ordered Hubble-type galaxies, they do not require additional angular momentum. We predict that through the consumption of their large gas reservoir, via the ongoing high levels of star formation, and the fragmentation of the clumpy  $\text{H II}$  regions, driven by the evolution in the characteristic star-forming clump mass (e.g. Livermore et al. 2012, 2015), the angular momentum of the galaxy is redistributed and the peculiar galaxies evolve to more stable and ordered Hubble-type morphologies.

We note that one possible origin for the peculiar morphology of high-redshift galaxies is galaxy interactions which disrupt the



steady-state dynamics and morphology of galaxies. Galaxy interactions and mergers are much more common in the distant Universe (Rodrigues et al. 2017) and would result in increased scatter in the  $j_* - M_*$  plane, depending on the magnitude of the merger and the gas fractions of the galaxies involved. We anticipate only the presence of extremely late state mergers in the KGES sample given the relatively small KMOS field of view and that we identify peculiar and disc galaxies to have comparable specific angular momentum and levels of turbulence.

## 5 CONCLUSIONS

We have analysed the distribution and correlations of the specific stellar angular momentum ( $j_*$ ) in typical  $z \sim 1.5$  star-forming galaxies by exploiting KMOS H $\alpha$  observations of 288 galaxies from the KGES Survey (Tiley et al., in preparation). The survey samples the star formation main-sequence with a broad range of stellar masses, from  $\log(M_*/M_\odot) = 8.9\text{--}11.7$  and H $\alpha$  star formation rates, with the sample having a 16–84th percentile range of  $\text{SFR} = 3\text{--}44 M_\odot \text{yr}^{-1}$ . We summarize our findings as follows:

(i) We use GALFIT to measure the structural properties for all 288 galaxies in the KGES survey from *HST* CANDELS (173 galaxies), archival (96 galaxies), and ground-based imaging (19 galaxies). We derive a median half-light radius of  $\langle R_h \rangle = 0.31 \pm 0.02$  ( $2.60 \pm 0.15$  kpc at  $z = 1.5$ ). We show that KGES galaxies occupy a similar parameter space to typical main-sequence galaxies in the stellar mass–stellar continuum half-light radius plane (Fig. 2).

(ii) We measure the CAS (concentration, asymmetry, and clumpiness) parameters of the galaxies in the KGES survey (Fig. 3) establishing a medium clumpiness of  $\langle S \rangle = 0.37 \pm 0.10$ , asymmetry of  $\langle A \rangle = 0.19 \pm 0.05$ , and a medium concentration of  $\langle C \rangle = 2.36 \pm 0.34$ . This is similar to the concentration and asymmetry parameters derived for typical main-sequence star-forming galaxies from  $z = 1.5$  to 3.6 by Law et al. (2012a) with  $A \sim 0.25$  and  $C \sim 3$ .

(iii) Taking advantage of the resolved dynamics for 235 galaxies in the sample, we derive the intrinsic H $\alpha$  rotation velocity of each galaxy. We combine the asymptotic rotation velocity and size to measure the specific stellar angular momentum and constrain the  $j_* - M_*$  plane for the KGES survey (Fig. 8). We quantify the plane with a function of the form  $\log_{10}(j_*) = 2.61 + 0.66(\log_{10}(M_*/M_\odot) - 10.10)$ . The normalization ( $\alpha = 2.61$ ) of this plane is lower than that of  $z \sim 0$  disc galaxies presented in Romanowsky & Fall (2012).

(iv) To quantify a galaxy’s position in the  $j_* - M_*$  plane we define a new parameter ( $\Delta j$ ) that is the residual of the logarithm of a galaxy’s specific stellar angular momentum and the logarithm of the specific stellar angular momentum of the parametric fit at the same stellar mass. We explore correlations between  $\Delta j$  and a galaxy’s velocity dispersion ( $\sigma_0$ ), establishing no correlation, as well with the ratio of rotation velocity to velocity dispersion ( $V(r = 2R_h/\sigma_0)$ ), and H $\alpha$  star formation rate surface density ( $\Sigma_{\text{SFR}}$ , Fig. 9).

(v) Galaxies with higher  $\Sigma_{\text{SFR}}$  tend to be more dispersion dominated and have lower angular momentum together with visual morphologies resembling spheroidal systems. Rotation-dominated galaxies, with low  $\Sigma_{\text{SFR}}$ , have higher angular momentum and have morphologies that resemble discs or peculiar systems.

(vi) To understand the connection between a galaxy’s morphology and specific stellar angular momentum, we take advantage of the multiband *HST* CANDELS imaging and derive WFC colour images. In Fig. 10, we show the  $j_* - M_*$  plane coloured by Hubble

morphology. We identify a trend of spheroidal galaxies having low angular momentum while the more ‘discy’ late-type morphology galaxies have higher angular momentum.

(vii) We explore the correlation between  $\Delta j$  and a galaxy’s parametrized morphology, establishing that higher Sérsic index, higher stellar bulge to total ratio, galaxies have lower angular momentum, while higher angular momentum galaxies have more clumpy morphologies. We propose a picture whereby at a fixed stellar mass spheroidal galaxies have lower angular momentum and are smooth and more symmetrical. Peculiar and disc-like galaxies have higher angular momentum and are much more clumpy.

(viii) We differentiate peculiar galaxies from disc-dominated systems at a fixed stellar mass by analysing their dynamical properties (Fig. 12). We derive a median Toomre  $Q_{\text{gas}}$  of  $\langle Q_{\text{gas}} \rangle = 0.66 \pm 0.01$  for all 243 KGES galaxies. Peculiar galaxies have higher  $\Sigma_{\text{SFR}}$ , and thus imply higher gas fractions than disc galaxies.

Overall, we have identified that the morphologies of high-redshift star-forming galaxies are more complicated than those in the local Universe, but can be split into three broad classes of spheroidal, disc, and peculiar. We can dynamically differentiate the three classes at fixed stellar mass, whereby spheroidal galaxies have lower specific angular momentum and high gas fractions, while disc-like galaxies have high specific angular momentum and lower gas fractions. Peculiar systems have equally high levels of specific angular momentum as disc galaxies, but have higher gas fractions.

In order to further explore these correlations and establish empirical constraints on how the gas fractions, stellar population demographic, and rotation curve gradients define the emergence of peculiar gas-rich systems, as well as Hubble-type spirals, we require accurate measurements of gas fractions in these systems e.g. ALMA molecular gas observations, as well as constraints on the metallicity and stellar age of galaxies from multiline emission line diagnostics.

## ACKNOWLEDGEMENTS

This work was supported by the Science and Technology Facilities Council (ST/L00075X/1). SG acknowledges the support of the Science and Technology Facilities Council through grant ST/N50404X/1 for support. EI acknowledges partial support from FONDECYT through grant N° 1171710. We thank the FMOS-COSMOS team for their invaluable contributions to the KGES target selection. ALT acknowledges support from STFC (ST/L00075X/1 and ST/P000541/1), ERC Advanced Grant DUSTYGAL (321334), and a Forrest Research Foundation Fellowship. LC is the recipient of an Australian Research Council Future Fellowship (FT180100066) funded by the Australian Government. Parts of this research were conducted by the Australian Research Council Centre of Excellence for All Sky Astrophysics in 3 Dimensions (ASTRO 3D), through project number CE170100013.

The KMOS data in this paper were obtained at the Very Large Telescope of the European Southern Observatory, Paranal, Chile (ESO Programme IDs 095.A-0748, 096.A-0200, 097.A-0182, 098.A-0311, and 0100.A-0134). This work is based in part on data obtained as part of the UKIRT Infrared Deep Sky Survey. This work is based on observations taken by the CANDELS Multi-Cycle Treasury Program with the NASA/ESA *HST*, which is operated by the Association of Universities for Research in Astronomy, Inc., under NASA contract NAS5-26555. *HST* data were also obtained from the data archive at the Space Telescope Science Institute.



## REFERENCES

- Abraham R. G., van den Bergh S., Glazebrook K., Ellis R. S., Santiago B. X., Surma P., Griffiths R. E., 1996, *ApJS*, 107, 1
- Almaini O. et al., 2007, in Metcalfe N., Shanks T., eds, ASP Conf. Ser. Vol. 379, Cosmic Frontiers. Astron. Soc. Pac., San Francisco, p. 163
- Behroozi P., Wechsler R. H., Hearin A. P., Conroy C., 2019, *MNRAS*, 488, 3143
- Benson A. J., Bower R. G., Frenk C. S., Lacey C. G., Baugh C. M., Cole S., 2003, *ApJ*, 599, 38
- Bouché N. et al., 2007, *ApJ*, 671, 303
- Bournaud F. et al., 2014, *ApJ*, 780, 57
- Bruce V. A. et al., 2014, *MNRAS*, 444, 1660
- Burkert A. et al., 2016, *ApJ*, 826, 214
- Calzetti D., Armus L., Bohlin R. C., Kinney A. L., Koornneef J., Storchi-Bergmann T., 2000, *ApJ*, 533, 682
- Catelan P., Theuns T., 1996, *MNRAS*, 282, 436
- Chabrier G., 2003, *PASP*, 115, 763
- Conselice C. J., 2003, *ApJS*, 147, 1
- Conselice C. J., 2014, *ARA&A*, 52, 291
- Conselice C. J., Bluck A. F. L., Ravindranath S., Mortlock A., Koekemoer A. M., Buitrago F., Grützbauch R., Penny S. J., 2011, *MNRAS*, 417, 2770
- Contini T. et al., 2016, *A&A*, 591, A49
- Cortese L. et al., 2014, *ApJ*, 795, L37
- Cortese L. et al., 2016, *MNRAS*, 463, 170
- Cowie L. L., Hu E. M., Songaila A., 1995, *Nature*, 377, 603
- Crain R. A. et al., 2015, *MNRAS*, 450, 1937
- D'Onghia E., Burkert A., Murante G., Khochfar S., 2006, *MNRAS*, 372, 1525
- da Cunha E., Charlot S., Elbaz D., 2008, *MNRAS*, 388, 1595
- da Cunha E. et al., 2015, *ApJ*, 806, 110
- Di Teodoro E. M., Fraternali F., Miller S. H., 2016, *A&A*, 594, A77
- Dimauro P. et al., 2018, *MNRAS*, 478, 5410
- El-Badry K. et al., 2018, *MNRAS*, 473, 1930
- ESO CPL Development Team, 2015, Astrophysics Source Code Library, record ascl:1504.003
- Falcón-Barroso J., Lyubenova M., van de Ven G., 2015, in Cappellari M., Courteau S., eds, Proc. IAU Symp. 311, Galaxy Masses as Constraints of Formation Models. Kluwer, Dordrecht, p. 78
- Fall S. M., 1983, in Athanassoula E., ed., Proc. IAU Symp. 100, Internal Kinematics and Dynamics of Galaxies. Kluwer, Dordrecht, p. 391
- Fall S. M., Efstathiou G., 1980, *MNRAS*, 193, 189
- Fall S. M., Romanowsky A. J., 2013, *ApJ*, 769, L26
- Fall S. M., Romanowsky A. J., 2018, *ApJ*, 868, 133
- Förster Schreiber N. M. et al., 2006, *ApJ*, 645, 1062
- Freeman K. C., 1970, *ApJ*, 160, 811
- Freundlich J. et al., 2013, *A&A*, 553, A130
- Garrison-Kimmel S. et al., 2018, *MNRAS*, 481, 4133
- Genzel R. et al., 2011, *ApJ*, 733, 101
- Giacconi R. et al., 2001, *ApJ*, 551, 624
- Gillman S. et al., 2019, *MNRAS*, 477
- Gnedin N. Y., Kravtsov A. V., 2010, *ApJ*, 714, 287
- Grogin N. A. et al., 2011, *ApJS*, 197, 35
- Guthrie B. N. G., 1992, *A&AS*, 93, 255
- Hammer F., Images Collaboration, 2009, in Jogee S., Marinova I., Hao L., Blanc G. A., eds, ASP Conf. Ser. Vol. 419, Galaxy Evolution: Emerging Insights and Future Challenges. Astron. Soc. Pac., San Francisco, p. 66
- Harrison C. M. et al., 2017, *MNRAS*, 467, 1965
- Hernandez X., Cervantes-Sodi B., 2006, *Rev. Mex. Astron. Astrofis.*, 26, 97
- Hernandez X., Park C., Cervantes-Sodi B., Choi Y.-Y., 2007, *MNRAS*, 375, 163
- Hinshaw G. et al., 2013, *ApJS*, 208, 19
- Hopkins P. F., Kereš D., Oñorbe J., Faucher-Giguère C.-A., Quataert E., Murray N., Bullock J. S., 2014, *MNRAS*, 445, 581
- Hopkins P. F. et al., 2018, *MNRAS*, 480, 800
- Hsieh B.-C., Wang W.-H., Hsieh C.-C., Lin L., Yan H., Lim J., Ho P. T. P., 2012, *ApJS*, 203, 23
- Hubble E. P., 1926, *ApJ*, 64, 321
- Huertas-Company M. et al., 2015, *ApJ*, 809, 95
- Jadhav Y. V., Banerjee A., 2019, *MNRAS*, 488, 547
- Jeans J. H., 1902, *Phil. Trans. R. Soc.*, 199, 1
- Johnson H. L. et al., 2018, *MNRAS*, 474, 5076
- Kartaltepe J. S. et al., 2015, *ApJ*, 221, 11
- Kennicutt Robert C. J., 1998, *ApJ*, 498, 541
- Koekemoer A. M. et al., 2007, *ApJS*, 172, 196
- Koekemoer A. M. et al., 2011, *ApJS*, 197, 36
- Krumholz M. R., Burkhard B., 2016, *MNRAS*, 458, 1671
- Lagos C. d. P., Theuns T., Stevens A. R. H., Cortese L., Padilla N. D., Davis T. A., Contreras S., Croton D., 2017, *MNRAS*, 464, 3850
- Lang P. et al., 2014, *ApJ*, 788, 11
- Lawrence A. et al., 2007, *MNRAS*, 379, 1599
- Law D. R., Steidel C. C., Shapley A. E., Nagy S. R., Reddy N. A., Erb D. K., 2012a, *ApJ*, 745, 85
- Law D. R., Steidel C. C., Shapley A. E., Nagy S. R., Reddy N. A., Erb D. K., 2012b, *ApJ*, 759, 29
- Livermore R. C. et al., 2012, *MNRAS*, 427, 688
- Livermore R. C. et al., 2015, *MNRAS*, 450, 1812
- Marasco A., Fraternali F., Posti L., Ijtsma M., Di Teodoro E. M., Oosterloo T., 2019, *A&A*, 621, L6
- Marshall M. A., Mutch S. J., Qin Y., Poole G. B., Wyithe J. S. B., 2019, *MNRAS*, 488, 1941
- Massey R., Stoughton C., Leauthaud A., Rhodes J., Koekemoer A., Ellis R., Shaghoulouian E., 2010, *MNRAS*, 401, 371
- McCracken H. J. et al., 2012, *A&A*, 544, A156
- Miller S. H., Bundy K., Sullivan M., Ellis R. S., Treu T., 2011, *ApJ*, 741, 115
- Mobasher B. et al., 2015, *ApJ*, 808, 101
- Mo H. J., Mao S., White S. D. M., 1998, *MNRAS*, 295, 319
- Muzzin A., Marchesini D., van Dokkum P. G., Labbé I., Kriek M., Franx M., 2009, *ApJ*, 701, 1839
- Muzzin A. et al., 2013, *ApJS*, 206, 8
- Obreschkow D., Glazebrook K., 2014, *ApJ*, 784, 26
- Obreschkow D. et al., 2015, *ApJ*, 815, 97
- Obreschkow D., Glazebrook K., Kilborn V., Lutz K., 2016, *ApJ*, 824, L26
- Okamoto T., Eke V. R., Frenk C. S., Jenkins A., 2005, *MNRAS*, 363, 1299
- Oklopčić A., Hopkins P. F., Feldmann R., Kereš D., Faucher-Giguère C.-A., Murray N., 2017, *MNRAS*, 465, 952
- Orr M. E. et al., 2018, *MNRAS*, 478, 3653
- Osterbrock D. E., Ferland G. J., 2006, Astrophysics of Gaseous Nebulae and Active Galactic Nuclei, University Science Books, Sausalito, CA
- Peebles P. J. E., 1969, *ApJ*, 155, 393
- Peng C. Y., Ho L. C., Impey C. D., Rix H.-W., 2011, Astrophysics Source Code Library, record ascl:1104.010
- Pforr J., Maraston C., Tonini C., 2012, *MNRAS*, 422, 3285
- Posti L., Fraternali F., Di Teodoro E. M., Pezzulli G., 2018, *A&A*, 612, L6
- Posti L., Marasco A., Fraternali F., Famaey B., 2019, *A&A*, 629, A59
- Puech M., Hammer F., Lehnert M. D., Flores H., 2007, *A&A*, 466, 83
- Puech M., Flores H., Rodrigues M., Hammer F., Yang Y. B., 2019, *MNRAS*, 488, 876
- Rodrigues M., Hammer F., Flores H., Puech M., Athanassoula E., 2017, *MNRAS*, 465, 1157
- Rodriguez-Gomez V. et al., 2017, *MNRAS*, 467, 3083
- Romanowsky A. J., Fall S. M., 2012, *ApJS*, 203, 17
- Romeo A. B., Mogotsi K. M., 2018, *MNRAS*, 480, L23
- Romeo A. B., Wiegert J., 2011, *MNRAS*, 416, 1191
- Sachdeva S., Gogoi R., Saha K., Kembhavi A., Raychaudhury S., 2019, *MNRAS*, 487, 1795
- Sales L. V., Navarro J. F., Schaye J., Dalla Vecchia C., Springel V., Booth C. M., 2010, *MNRAS*, 409, 1541
- Sandage A., 1986, Star-forming Dwarf Galaxies and Related Objects. p. 31
- Sandage A., Freeman K. C., Stokes N. R., 1970, *ApJ*, 160, 831
- Schaye J. et al., 2015, *MNRAS*, 446, 521
- Schreiber C. et al., 2015, *A&A*, 575, A74
- Scoville N. et al., 2007, *ApJS*, 172, 1

- Sharda P., Federrath C., da Cunha E., Swinbank A. M., Dye S., 2018, *MNRAS*, 477, 4380
- Sharma M., Theuns T., 2019, *MNRAS*, preprint ([arXiv:1906.10135](https://arxiv.org/abs/1906.10135))
- Sharples R. et al., 2013, *The Messenger*, 151, 21
- Snyder G. F. et al., 2015, *MNRAS*, 454, 1886
- Sofue Y., Rubin V., 2001, *ARA&A*, 39, 137
- Sokołowska A., Capelo P. R., Fall S. M., Mayer L., Shen S., Bonoli S., 2017, *ApJ*, 835, 289
- Soto K. T., Lilly S. J., Bacon R., Richard J., Conseil S., 2016, *MNRAS*, 458, 3210
- Stewart K. R. et al., 2017, *ApJ*, 843, 47
- Stott J. P. et al., 2016, *MNRAS*, 457, 1888
- Sweet S. M., Fisher D. B., Glazebrook K., Obreschkow D., Lagos C. D. P., Wang L., 2018, preprint ([arXiv:1808.06269](https://arxiv.org/abs/1808.06269))
- Sweet S. M. et al., 2019, *MNRAS*, 485, 5700
- Swinbank A. M. et al., 2017, *MNRAS*, 467, 3140
- Tacchella S. et al., 2019, *MNRAS*, 487, 1573
- Thob A. C. R. et al., 2019, *MNRAS*, 485, 972
- Tiley A. L. et al., 2019, *MNRAS*, 482, 2166
- Tissera P. B., Lambas D. G., 1990, *MNRAS*, 246, 151
- Toomre A., 1964, *ApJ*, 139, 1217
- Trayford J. W., Frenk C. S., Theuns T., Schaye J., Correa C., 2018, *MNRAS*, 483, 2761
- Tully R. B., Fisher J. R., 1977, *A&A*, 500, 105
- Turner O. J. et al., 2017, *MNRAS*, 471, 1280
- Übler H. et al., 2019, *ApJ*, 880, 48
- van der Wel A. et al., 2012, *ApJS*, 203, 24
- van der Wel A. et al., 2014, *ApJ*, 788, 28
- Wang B., Silk J., 1994, *ApJ*, 427, 759
- Weijmans A.-M. et al., 2014, *MNRAS*, 444, 3340
- Weijmans A.-M., MaNGA Team, 2016, in Skillen I., Barcells M., Trager S., eds, *ASP Conf. Ser. Vol. 507, Multi-Object Spectroscopy in the Next Decade: Big Questions, Large Surveys, and Wide Fields*. Astron. Soc. Pac., San Francisco, p. 257
- Wisnioski E. et al., 2015, *ApJ*, 799, 209
- Wuyts S. et al., 2013, *ApJ*, 779, 135
- Zoldan A., De Lucia G., Xie L., Fontanot F., Hirschmann M., 2018, *MNRAS*, 481, 1376
- Zoldan A., De Lucia G., Xie L., Fontanot F., Hirschmann M., 2019, *MNRAS*, 487, 1635

## SUPPORTING INFORMATION

Supplementary data are available at *MNRAS* online.

### Appendix A: SEDs, *HST* Imaging and Kinematics

### Appendix B: GALFIT Model Examples

Please note: Oxford University Press is not responsible for the content or functionality of any supporting materials supplied by the authors. Any queries (other than missing material) should be directed to the corresponding author for the article.

This paper has been typeset from a  $\text{\TeX}/\text{\LaTeX}$  file prepared by the author.